https://doi.org/10.5194/tc-2021-116
Preprint. Discussion started: 30 April 2021

The Cryosphere Discussions

An empirical algorithm to map perennial firn aquifers, ice slabs, and perched firn aquifers within the Greenland Ice Sheet using satellite L-band microwave radiometry

Julie Z. Miller[1,2], Riley Culberg[3], David G. Long[4], Christopher A. Shuman[5], Dustin M. Schroeder[3,6], Mary J. Brodzik[1,7]

[1] Cooperative Institute for Research in Environmental Sciences, University of Colorado, Boulder, Colorado, USA
[2] Earth Science and Observation Center, University of Colorado, Boulder, Colorado, USA
[3] Department of Electrical Engineering, Stanford University, Stanford, California, USA
[4] Department of Electrical and Computer Engineering, Brigham Young University, Provo, Utah, USA
[5] University of Maryland, Baltimore County, Joint Center for Earth Systems Technology at Code 615, Cryospheric Sciences Laboratory NASA Goddard Space Flight Center, Greenbelt, Maryland, USA
[6] Department of Geophysics, Stanford University, Stanford, CA, USA
[7] National Snow and Ice Data Center, University of Colorado, Boulder, Colorado, USA
Correspondence to: jzmiller.research@gmail.com

Abstract

Perennial firn aquifers are subsurface meltwater reservoirs formed from a water-saturated firn layer. They have been observed within the percolation facies of glaciated regions experiencing intense seasonal surface melting and high snow accumulation. Widespread perennial firn aquifers have been identified within the Greenland Ice Sheet (GrIS) via field expeditions, airborne ice-penetrating radar surveys, and satellite microwave sensors. In contrast, ice slabs are nearly-continuous ice layers that form on spatial scales of kilometers as a result of surface and subsurface water-saturated snow and firn layers sequentially refreezing following multiple melting seasons. They have been observed within the percolation facies of glaciated regions experiencing intense seasonal surface melting, but in areas where snow accumulation is at least ~25% lower as compared to perennial firn aquifer areas. Widespread ice slabs have recently been identified within the GrIS via field expeditions and airborne ice-penetrating radar surveys, specifically in areas where perennial firn aquifers typically do not form. However, ice slabs have yet to be inferred from space. Together, these two ice sheet features represent distinct, but related, sub-facies within the broader percolation facies of the GrIS that can be defined primarily by differences in snow accumulation, which influences the englacial hydrology and thermal characteristics of firn layers at depth.

Here, for the first time, we use enhanced-resolution vertically-polarized L-band brightness temperature (T_V^B) imagery (2015-2019) generated using observations collected over the GrIS by NASA's Soil Moisture Active Passive (SMAP) satellite to map both perennial firn aquifer and ice slab areas as a continuous system over the percolation facies. We also map 'perched' firn aquifer areas, which we define as areas where shallow water-saturated firn layers transiently form on top of buried ice slabs, or other semi-impermeable layers within the snow and firn. An empirical algorithm

https://doi.org/10.5194/tc-2021-116
Preprint. Discussion started: 30 April 2021

The Cryosphere Discussions
Open Access
EGU

previously developed to map the extent of Greenland's perennial firn aquifers via fitting exponentially decreasing temporal L-band signatures to a set of sigmoidal curves is recalibrated to also map the extent of ice slab and perched firn aquifer areas using airborne ice-penetrating radar surveys collected by NASA's Operation Ice Bridge (OIB) campaigns (2010-2017). Our SMAP-derived maps show that between 2015 and 2019, perennial firn aquifer areas extended over ~64,000 km^2, ice slab areas extended over ~76,000 km^2, and perched firn aquifer areas extended over ~37,000 km^2. Combined together, these three sub-facies are the equivalent of ~24% of the percolation facies of the GrIS. As Greenland's climate continues to warm, and seasonal surface melting increases in extent, intensity, and duration, quantifying the possible rapid expansion of each of these sub-facies using satellite L-band microwave radiometry has significant implications for understanding ice sheet-wide variability in englacial firn hydrology resulting in meltwater-induced hydrofracturing and accelerated ice flow as well as high-elevation run-off that can impact the mass balance and stability of the GrIS.

1 Introduction

The recent launch of several satellite L-band microwave radiometry missions by NASA (Aquarius mission, Levine, et al., 2007; Soil Moisture Active Passive (SMAP) mission, Entekhabi et al., 2010) and ESA (Soil Moisture and Ocean Salinity (SMOS), Kerr et al., 2010) has provided a new Earth-observation tool capable of detecting stored meltwater ~tens of meters to kilometers beneath the surface of ice sheets. Jezek et al. (2015) recently demonstrated that in the high-elevation (~3500 m.a.s.l.) dry snow facies of the Antarctic Ice Sheet, meltwater stored in subglacial Lake Vostok can be detected ~4000 m beneath the ice sheet surface. Subglacial lakes represent radiometrically cold subsurface meltwater reservoirs. Upwelling L-band emissions from the radiometrically warm bedrock underlying the subglacial lakes are effectively blocked by high reflectivity and attenuation at the interface between bedrock and the overlying lake bottom. This results in a lower observed microwave brightness temperature (T^B) at the ice sheet surface as compared to other dry snow facies areas where bedrock contributes to L-band emissions depth-integrated over the entire ice sheet thickness.

Similar to subglacial lakes, perennial firn aquifers also represent radiometrically cold subsurface meltwater reservoirs (Miller et al., 2020) formed from a ~4 m-25 m thick water-saturated firn layer (Koenig et al., 2014; Montgomery et al., 2017; Chu et al., 2018). They have been observed via field expeditions and airborne ice-penetrating radar surveys in the lower-elevation (< ~2000 m.a.s.l.) percolation facies of the Greenland Ice Sheet (GrIS), at depths from between ~1 m and 40 m beneath the ice sheet surface (Miège et al. 2016), and in areas that experience intense seasonal surface melting (>650 mm yr^{-1}) during the melting season and high snow accumulation (>800 mm yr^{-1}) during the freezing season (Forster et al., 2014). High snow accumulation in perennial firn aquifer areas thermally insulates water-saturated firn layers from the cold atmosphere allowing seasonal meltwater to be stored in liquid form if the overlying seasonal snow layer is sufficiently thick (Kuipers Munneke et al., 2014). Koenig et al. (2014) estimated that the

https://doi.org/10.5194/tc-2021-116
Preprint. Discussion started: 30 April 2021

volumetric fraction of meltwater stored within the pore space of Greenland's perennial firn aquifers just prior to melt onset ranges from between ~10% and 25%, which limits the upward propagation of electromagnetic energy from greater depths within the ice sheet. Large volumetric fractions of meltwater within the firn pore space results in high reflectivity and attenuation at the interface between water-saturated firn layers and the overlying refrozen firn layers, and between glacial ice or a semi-impermeable layer and the overlying water-saturated firn layers. Upwelling L-band emissions from deeper glacial ice and the underlying bedrock are effectively blocked.

While perennial firn aquifers are radiometrically cold, the slow refreezing of deeper firn layers saturated with large volumetric fractions of meltwater represents a significant source of latent heat that is continuously released throughout the freezing season. Refreezing of seasonal meltwater by the descending winter cold wave (Pfeffer et al., 1991), and the subsequent formation of embedded ice structures (i.e., horizontally-oriented ice layers and ice lenses, and vertically-oriented ice pipes; Benson et al., 1960; Humphrey et al., 2012; Harper et al., 2012) within the upper snow and firn layers represents a secondary source of latent heat. These heat sources help maintain meltwater at depth. Perennial firn aquifer areas are radiometrically warmer than other percolation facies areas where the single source of latent heat is via refreezing of seasonal meltwater. This results in a higher observed T^B at the ice sheet surface during the freezing season as compared to other percolation facies areas where seasonal meltwater is fully refrozen and stored exclusively as embedded ice.

Many open questions remain about Greenland's perennial firn aquifers, regarding initial formation, extent, depth, flow characteristics, timescales of refreezing and/or englacial drainage, and connections to the subglacial hydrological system. Seasonal surface melting over the GrIS has increased in extent, intensity, and duration since the beginning of the satellite era (Steffen et al., 2004; Tedesco e al., 2008; Tedesco et al., 2011; Nghiem et al., 2012; Tedesco et al., 2016; Tedesco and Fettweis, 2020; Cullather et al., 2020). If this trend continues (Franco et al., 2013; Noël et al., 2021), subsequent increases in the volume of meltwater stored within Greenland's perennial firn aquifers will increase the possibility of crevasse-deepening via meltwater-induced hydrofracturing (Alley et al., 2005; van der Veen, 2007), especially if crevasse fields laterally expand into perennial firn aquifer areas as a result of accelerated ice flow (Colgan et al., 2016). Meltwater-induced hydrofracturing is an important component of supraglacial lake drainage during the melting season (Das et al., 2008; Stevens et al., 2015) leading to at least temporary accelerated flow velocities (Zwally et al., 2002; Joughin et al., 2013; Moon et al., 2014) and mass balance changes (Joughin et al., 2008). Greenland's firn perennial aquifers may also support meltwater-induced hydrofracturing, even during the freezing season (Poinar et al., 2017; 2019).

Recently, mapping the extent of Greenland's perennial firn aquifers from space was demonstrated using satellite L-band microwave radiometry (Miller et al., 2020). Exponentially decreasing temporal L-band signatures observed in enhanced-resolution vertically-polarized L-band brightness temperature (T_V^B) imagery (2015-2016) generated using observations collected over the GrIS by the microwave radiometer on the SMAP satellite (Brodzik et al., 2019) were correlated with a single year of perennial firn aquifer

https://doi.org/10.5194/tc-2021-116
Preprint. Discussion started: 30 April 2021

The Cryosphere Discussions
Open Access
EGU

detections (2016) identified via the Center for Remote Sensing of Ice Sheets (CReSIS) Multi-Channel Coherent Radar Depth Sounder (MCoRDS) flown by NASA's Operation Ice Bridge (OIB) campaigns (Miège et al. 2016; Rodriguez-Morales et al, 2014). An empirical algorithm to map extent was developed by fitting temporal L-band signatures to a set of sigmoidal curves derived from the continuous logistic model.

The relationship between the radiometric, and thus the physical, temperature of perennial firn aquifer areas, as compared to other percolation facies areas, forms the basis of the empirical algorithm. Miller et al. (2020) hypothesized that the dominant control on the relatively slow exponential rate of T_V^B decrease over perennial firn aquifer areas is physical temperature versus depth. L-band emissions from the radiometrically warm upper snow and firn layers decrease during the freezing season as embedded ice structures slowly refreeze at increased depths below the ice sheet surface. In the percolation facies, refreezing of seasonal meltwater results in the formation of an intricate network of embedded ice structures that are large (~10-100 cm long, ~10-20 cm wide; Jezek et al., 1994) relative to the L-band wavelength (~21 cm). Embedded ice structures induce strong volume scattering (Rignot et al., 1993; Rignot 1995) that decreases T^B (Zwally, 1977; Swift et al. 1985; Jezek et al., 2018).

Ice slabs are ~1 m–16 m thick nearly-continuous ice layers that form on spatial scales of kilometers as a result of surface and subsurface water-saturated snow and firn layers sequentially refreezing following multiple melting seasons (Machguth et al., 2016; McFerrin et al., 2019). Over time, they become dense low-permeability solid-ice layers overlying deeper permeable firn layers. Similar to perennial firn aquifers, ice slabs have been observed via field expeditions and ice-penetrating airborne radar surveys in the lower-elevation (< ~2000 m.a.s.l.) percolation facies of the GrIS. They form at depths from between ~1 m and 20 m beneath the ice sheet surface. Particularly in areas that experience intense seasonal surface melting (>600 mm yr−1) during the melting season, and lower snow accumulation (<600 mm yr−1) during the freezing season as compared to perennial firn aquifer areas (McFerrin et al., 2019). Lower snow accumulation in ice slab areas results in a seasonal snow layer that is insufficiently thick to thermally insulate water-saturated firn layers and seasonal meltwater is instead stored as embedded ice. Refreezing of seasonal meltwater by the descending winter cold wave, and the subsequent formation of ice slabs as well as other embedded ice structures within the upper snow and firn layers is the single source of latent heat in ice slab areas. While ice slab areas are radiometrically warmer than other percolation facies areas with a lower volumetric fraction of embedded ice, they are radiometrically colder than perennial firn aquifer areas. This results in a lower observed T^B at the ice sheet surface during the freezing season.

Consistent with recent seasonal surface melting trends, meltwater run-off has accelerated to become the dominant mass loss mechanism over the GrIS (van den Broeke et al., 2016). However, significant uncertainty remains in meltwater run-off estimates in the percolation facies as a result of the lack of knowledge of heterogeneous infiltration processes within the snow and firn layers (Pfeffer and Humphrey, 1996), the depths to which meltwater can descend beneath the ice sheet surface (Humphrey et al., 2012), and the formation of englacial firn hydrological features (Benson et al., 1960; Humphrey et al., 2012; Forster et al., 2014), especially ice layers and ice slabs (Machguth et al., 2016, McFerrin et al., 2019; Culberg et

https://doi.org/10.5194/tc-2021-116
Preprint. Discussion started: 30 April 2021

al., 2021). A notable example of this lack of knowledge is the identification by Forster et al., (2014) of widespread perennial firn aquifers within the percolation facies of the GrIS via airborne ice-penetrating radar surveys collected by NASA's OIB campaigns (2010-2014; Rodriguez-Morales et al, 2014) that store large volumes (~140 Gt; Koenig et al., 2014) of meltwater that was previously unknown. The mapped extent (2010-2014) shown in Forster et al., (2014) can be distinctly observed in 1978 enhanced resolution Ku-band radar backscatter imagery (Long and Drinkwater, 1994) collected by the radar scatterometer on NASA's first Earth-observing satellite - the Seasat-A mission (Jones et al., 1982). This suggests that Greenland's perennial firn aquifers have likely existed undetected in the deeper firn layers of the percolation facies for decades. Meltwater storage in both solid (i.e., embedded ice structures) and liquid (i.e., perennial firn and perched firn aquifers) form can buffer meltwater run-off in the percolation facies (Harper et al., 2012). However, the formation of near-surface ice layers and ice slabs reduces the pore space within the upper snow and firn layers and facilitates lateral meltwater flow with minimum vertical percolation into the deeper firn layers, thus enhancing meltwater run-off downslope towards the periphery. Lateral meltwater flow across ice layers overlying deeper permeable firn layers was first postulated by Müller (1962). The theory was then further developed by Pfeffer et al., (1991) as an end-member case for meltwater run-off, with the other end member case being lateral meltwater flow across superimposed ice in the wet snow facies and/or across glacial ice in the ablation facies. McFerrin et al., (2019) recently identified widespread near-surface ice slabs within the percolation facies of the GrIS via airborne ice-penetrating radar surveys collected by NASA's OIB campaigns (2010-2014; Rodriguez-Morales et al, 2014). Lateral meltwater flow and high-elevation (~1850 m.a.s.l) meltwater run-off across the identified ice slabs was also observed in visible satellite imagery collected by the NASA-USGS Landsat 7 mission (e.g. Goward et al., 2001). This was also observed during the anomalous 2012 melting season (McFerrin et al., 2019) during which seasonal surface melting extended over ~99% of the GrIS (Nghiem et al., 2012)

In this study, we use enhanced-resolution L-band T_V^B imagery (2015-2019) generated using observations collected over the GrIS by the microwave radiometer on the SMAP satellite (Brodzik et al., 2019) to map ice sheet-wide englacial firn hydrological features within the percolation facies. First, we adapt our empirical algorithm to map the extent of Greenland's perennial firn aquifers (Miller et al., 2020). We correlate exponentially decreasing temporal L-band signatures with five years of perennial firn aquifer detections (2010-2014) identified via the CReSIS Accumulation Radar (AR) flown by NASA's OIB campaigns (Miège et al. 2016), and three years of additional detections (2015-2017) more recently identified via MCoRDS (Miller et al., 2020). Next, we extend our empirical algorithm to also map the extent of ice slab and perched firn aquifer areas. We identify distinct temporal L-band signatures in T_V^B time series over ice slab detections (2010-2014) recently identified via AR (McFerrin et al., 2019). Similar to temporal L-band signatures over perennial firn aquifer areas, temporal L-band signatures over ice slab areas are exponentially decreasing during the freezing season, however, the rate of T_V^B decrease is slightly more rapid. We correlate these relatively rapidly exponentially decreasing temporal L-band signatures with five years of AR-derived ice slab detections. Additionally, we correlate exponentially decreasing temporal L-band signatures with AR- and MCoRDS-derived detections where perennial firn aquifer and ice slab areas overlap. We identify these transitional areas as perched firn aquifer areas. We infer that, in these areas, shallow water-saturated firn layers transiently form on top of buried ice slabs or other semi-impermeable layers, such as spatially coherent melt layers that form in the higher elevations (> ~2000 m.a.s.l.) of the percolation facies and the dry snow facies that were recently identified via AR (Culberg et al., 2021). Perched firn aquifers likely form during some melting seasons as a result of interannual variability in surface melting and snow accumulation, and the formation of englacial firn hydrological features. Finally, we re-calibrate the sigmoidal curves to map the extent of perennial firn aquifer, ice slab, and perched firn aquifer areas over the percolation facies of the GrIS

2 Methods

2.1 The Soil Moisture Active Passive (SMAP) Mission

The key science objectives of NASA's SMAP mission (https://smap.jpl.nasa.gov/) are to map terrestrial soil moisture and freeze/thaw state over Earth's land surfaces from space. However, the global L-band T^B observations collected by the SMAP satellite also have many cryospheric applications. Mapping ice sheet-wide englacial firn hydrological features over Earth's polar ice sheets represents an interesting analog and an innovative extension of the science objectives. Measurements of moisture (i.e., defined in this study in terms of the volumetric fraction of meltwater within the upper snow and firn layers of the percolation facies) and freeze-thaw state (i.e., defined in this study in terms of the firn saturation parameter (see Section 2.4.3) and the refreezing rate parameter (see Section 2.4.4)) are critical to understanding the hydrospheric state over Earth's polar ice sheets. Perennial firn aquifers, ice slabs, and perched firn aquifers represent recently identified components of the hydrosphere that are capable of storing large volumes of meltwater in both solid and liquid form that can initiate meltwater-induced hydrofracturing and accelerated ice flow as well as high-elevation run-off, and impact the mass balance and stability of the GrIS. Critically, the majority of meltwater is stored at depths that only L-band satellite microwave sensors (i.e., radiometers, radar scatterometers, and synthetic aperture radars) are capable of detecting.

Previous and current satellite microwave radiometer, radar scatterometer, and synthetic aperture radar missions that operate in the frequency range between 37 GHz (Ka-band) and 5.3 GHz (C-band) have provided a multi-decadal (1978-present) record of multi-frequency T^B and radar backscatter observations over Earth's polar ice sheets since the beginning of the satellite era. The most common geophysical parameter mapped over ice sheets using these observations is the extent of seasonal surface melting. The key difference between L-band and higher frequency satellite microwave sensors is penetration depth. When the snow and firn layers are saturated with meltwater during the melting season, the penetration depth of both L-band and higher frequency satellite microwave sensors is less than ~a meter. When surface and subsurface water-saturated snow and firn layers and embedded ice structures subsequently refreeze, the penetration depth of higher frequency satellite microwave sensors ranges from between ~centimeters and meters. During the freezing season, water-saturated snow and firn layers either completely refreeze

https://doi.org/10.5194/tc-2021-116
Preprint. Discussion started: 30 April 2021

(i.e., ice layers, ice slabs, spatially coherent melt layers) or underlay the refrozen upper snow and firn layers of the percolation facies and descend to depths ranging from between ~1 m and 40 m (Miège et al., 2016) beneath the ice sheet surface (i.e., perennial and perched firn aquifers). While the upper surface of stored meltwater in some perennial and perched firn aquifers may remain at depths that are shallow enough to be directly detected by C-band satellite microwave sensors, the mean depth just prior to melt onset (~22 m; Miège et al., 2016) is too deep to be detected at this wavelength. L-band satellite microwave sensors can detect perennial firn aquifers from as much as an order of magnitude deeper than can be observed by C-band satellite microwave radiometers. Deep enough to directly detect the upper surface of stored meltwater over the entire depth range mapped by airborne ice-penetrating radar surveys over the GrIS.

2.1 SMAP Enhanced-Resolution L-band T^B Imagery

NASA's SMAP satellite was launched 31 January 2015 and carries a microwave radiometer that operates at a frequency of 1.41 GHz (L-band) (Enkentabi et al., 2010). It is currently collecting observations of vertically and horizontally-polarized T^B over Greenland. The surface incidence angle is ~40°, and the radiometric accuracy is ~1.3 K (Piepmeier et al., 2017).

The Scatterometer Image Reconstruction (SIR) algorithm was developed to reconstruct coarse resolution satellite scatterometry imagery on a higher spatial resolution grid (Long et al., 1993; Early and Long, 2001). The SIR algorithm has been adapted for coarse resolution satellite microwave radiometry imagery (Long and Daum, 1998; Long and Brodzik, 2016; Long et al., 2019). The microwave radiometer form of the SIR algorithm (rSIR) exploits the measurement response function (MRF) for each observation, which is a smeared version of the antenna pattern. Using the overlapping MRFs, the rSIR algorithm reconstructs T^B from the spatially filtered low-resolution sampling provided by the observations. In effect, it generates an MRF-deconvolved T^B image. Combining multiple orbital passes increases the sampling density, which improves both the accuracy and resolution of SMAP enhanced-resolution T^B imagery (Long et al., 2019).

Over Greenland, the rSIR algorithm combines satellite orbital passes that occur between 8 a.m. and 4 p.m. local time-of-day to reconstruct SMAP enhanced-resolution T^B imagery twice-daily (i.e., morning and evening orbital pass interval, respectively). T^B imagery is projected on a Northern Hemisphere (NH) Equal-Area Scalable Earth Grid (EASE-Grid 2.0; Brodzik et al., 2012) at a 3.125 km rSIR grid cell spacing. The effective resolution for each grid cell is dependent on the number of observations used in the rSIR reconstruction and is coarser than the rSIR grid cell spacing. While the effective resolution of conventionally processed SMAP T^B imagery posted on a 25 km grid is ~30 km, the effective resolution of SMAP enhanced-resolution T^B imagery posted on a 3.125 km grid is ~18 km, an improvement of ~60% (Figs. 1; 2) (Long et al., 2020).

For our analysis of the percolation facies, we use SMAP enhanced-resolution T_V^B imagery over the GrIS. Compared to the horizontally-polarized channel, the vertically-polarized channel exhibits decreased sensitivity to variability in the volumetric fraction of meltwater, which is attributed to reflection coefficient

https://doi.org/10.5194/tc-2021-116
Preprint. Discussion started: 30 April 2021

differences between channels (Miller et al., 2020). Using the vertically polarized channel also results in a reduced chi-squared error statistic when fitting T_V^B time series to the sigmoid function (see Section 2.4.5). We construct T_V^B imagery that alternate morning and evening orbital pass observations annually, beginning and ending just prior to melt onset. The Greenland Ice Mapping Project (GIMP) Land Ice and Ocean Classification Mask and Digital Elevation Model (Howat et al., 2014) are projected on a NH EASE-Grid 2.0 at a 3.125 km rSIR grid cell spacing. T_V^B imagery between 1 April 2015 and 31 March 2019 are ice sheet-masked, and an elevation for each rSIR grid cell is calculated.

2.2 Airborne Ice-Penetrating Radar Surveys

Miller et al., (2020) calibrated the empirical algorithm to map the extent of Greenland's perennial firn aquifers by correlating a single year of exponentially decreasing temporal L-band signatures (2015-2016) with coincident perennial firn aquifer detections (2016) identified via MCoRDS. Here, we extend and expand the calibration of our adapted empirical algorithm to include four years of exponentially decreasing temporal L-band signatures (2015-2019) correlated with eight years of perennial firn aquifer detections (2010-2017) and five years of ice slab detections (2010-2014) identified via AR and MCoRDS (Fig. 1c). Our multi-year calibration technique projects perennial firn aquifer and ice slab detections on three separate NH EASE-Grids 2.0 at an rSIR grid cell spacing of 3.125 km, consistent with the rSIR grid cell spacing of the SMAP enhanced-resolution L-band T_V^B imagery. Interannual variability is not resolved in this study, however, it will be explored further in future work.

An advantage of the multi-year calibration technique as compared to the single-coincident year calibration technique (Miller et al., 2020) is that it increases the number of rSIR grid cells that can be assessed. It also provides repeat targets that can account for variability in the dielectric and geophysical properties that seasonally influence the radiometric temperature and temporal L-band signatures in stable perennial firn aquifer, ice slab, and perched firn aquifer areas. Uncertainty is introduced by correlating exponentially decreasing temporal L-band signatures with AR- and MCoRDS-derived detections that are not coincident in time. The multi-year calibration technique assumes the extent of each area remains stable, which is not necessarily the case as climate extremes (Cullather et al., 2020) can influence each of these sub-facies. The assumption of stability neglects boundary transitions in the extent of perennial firn aquifer areas associated with refreezing of shallow water-saturated firn layers, englacial drainage of meltwater into crevasses at the periphery (Poinar et al., 2017; Poinar et al, 2019), and transient upslope expansion (Montgomery et al., 2017). Once formed, ice slabs are essentially permanent features within the upper snow and firn layers of the percolation facies until they are compressed into glacial ice. However, they may transition into superimposed ice at the lower boundary of ice slab areas or rapidly expand upslope, particularly following extreme melting seasons (McFerrin et al., 2019). By our definition, perched firn aquifers are transient features. Thus, we simply consider our mapped extent a high-probability area for the preferential formation of each of these sub-facies within the broader percolation facies, with continued presence dependent on seasonal surface melting and snow accumulation in subsequent years.

https://doi.org/10.5194/tc-2021-116
Preprint. Discussion started: 30 April 2021

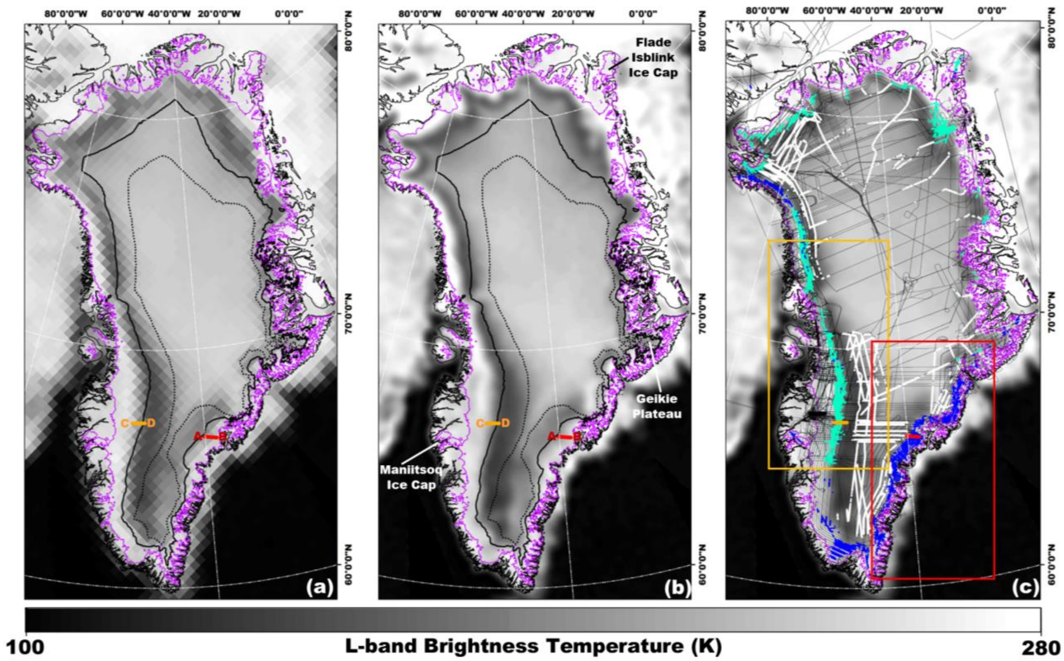

Figure 1

(a) Gridded (25 km), and (b) enhanced-resolution (3.125 km) L-band T_V^B imagery generated using observations collected 15 April 2016 by the microwave radiometer on the SMAP satellite during the evening orbital pass interval over Greenland (Brodzik et al., 2019). The solid black line is the 2000 m.a.s.l. contour, and the black dotted line is the 2500 m.a.s.l. contour (Howat et al., 2014). The purple line is the ice sheet extent (Howat et al., 2014). The black peripheral line is the coast of Greenland and adjacent Ellesmere Island (Wessel and Smith, 1996). The whiter regions of higher T_V^B over the high-elevation (> ~2500 m.a.s.l.) interior are the dry snow facies. The darker grey regions of lower T_V^B are the percolation facies, including ice slabs and perched firn aquifer areas. The whiter regions of higher T_V^B over the coastal areas, peripheral ice caps (e.g., Maniitsoq and Flade Isblink) and nearby islands are perennial firn aquifers, superimposed or glacial ice, land, or spatially integrated L-band emissions. The whiter regions of higher T_V^B outside the ice sheet extent are sea ice. (c) The SMAP enhanced-resolution L-band T_V^B imagery is overlaid with AR- and MCoRDS-derived 2010-2017 perennial firn aquifer (blue shading; Miège et al., 2016), 2010-2014 ice slab (cyan shading; McFerrin et al., 2019), and 2012 spatially coherent melt layer (white shading; Culberg et al., 2021) detections along OIB flight lines (black lines). Overlapping perennial firn aquifer and ice slab detections are interpreted as perched firn aquifer areas. The red and orange boxes in (c) are zoom areas over south eastern Greenland (Fig. 2a), and south western Greenland (Fig. 2b), respectively. The red line is AR radargram profile along perennial firn aquifer transect A-B (Fig. 3a). The orange line is AR radargram profile along ice slab transect C-D (Fig. 3b).

https://doi.org/10.5194/tc-2021-116
Preprint. Discussion started: 30 April 2021

The Cryosphere Discussions
Open Access
EGU

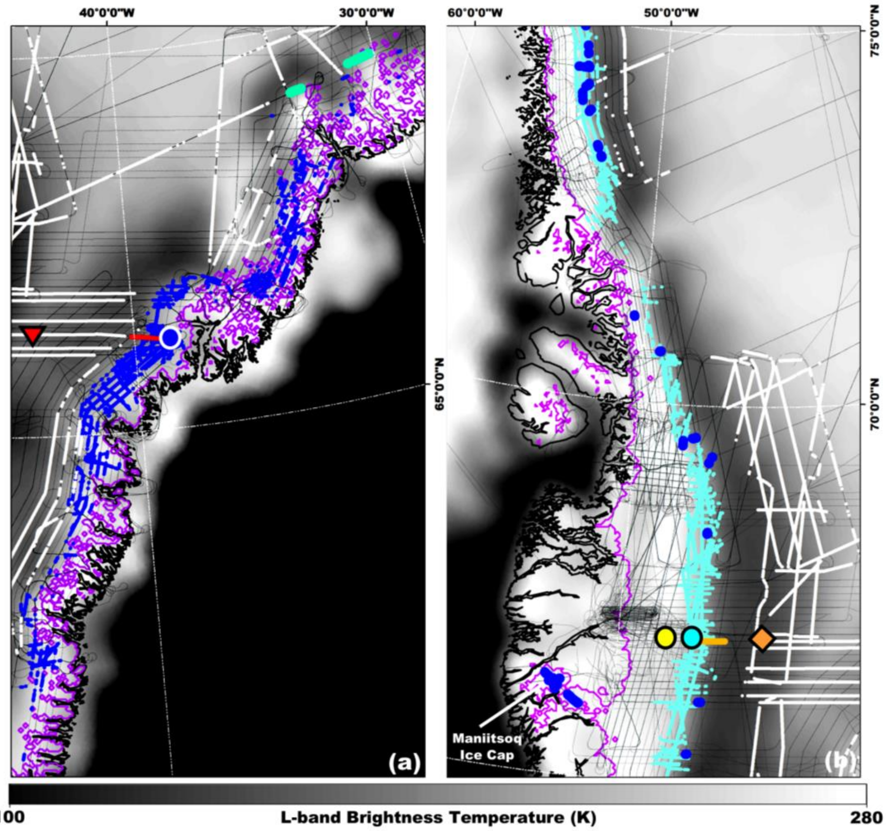

Figure 2

Enhanced-resolution (3.125 km) L-band T_V^B imagery generated using observations collected 15 April 2016 by the microwave radiometer on the SMAP satellite during the evening orbital pass interval over (a) south eastern Greenland (Fig. 1c; zoom area in red box), and (b) south western Greenland (Fig. 1c; zoom area in orange box) (Brodzik et al., 2019). The purple line is the ice sheet or ice cap extent (Howat et al., 2014). The black peripheral line is the coast (Wessel and Smith, 1996). (c) The SMAP enhanced-resolution L-band T_V^B imagery is overlaid with AR- and MCoRDS-derived 2010-2017 perennial firn aquifer (blue shading; Miège et al., 2016), 2010-2014 ice slab (cyan shading; McFerrin et al., 2019), and 2012 spatially coherent melt layer (white shading; Culberg et al., 2021) detections along OIB flight lines (black lines). Overlapping perennial firn aquifer and ice slab detections are interpreted as perched firn aquifer areas. The red line is AR radargram profile along perennial firn aquifer transect A-B (Figs. 1; 3a). The orange line is AR radargram profile along ice slab transect C-D (Figs. 1; 3b). The blue circle is a perennial firn aquifer area (Figs. 3a; 4a). The cyan circle is a perched firn aquifer area (Figs. 3b; 4b). The orange diamond is a percolation facies area (Fig. 4c). The red triangle is a high-elevation (~2500 m.a.s.l.) percolation facies area (Fig. 4d). The yellow circle is a superimposed ice area (Fig. 4e).

Annual perennial firn aquifer and ice slab detections that may introduce significant uncertainty into the multi-year calibration technique include those following the 2010 melting season, which was exceptionally long (Tedesco et al., 2010), the anomalous 2012 melting season (Nghiem et al., 2012), and the 2015 melting season which was especially intense in western and northern Greenland (Tedesco et al., 2016). Following these extreme melting seasons, significant changes in the dielectric and geophysical properties likely occurred across large portions of the GrIS, including perennial firn aquifer recharging resulting in increases in meltwater volume and decreases in the depth to the upper surface of stored meltwater. The formation of expansive near-surface ice slabs (McFerrin et al., 2019) likely resulted in the formation of more extensive perched firn aquifers during subsequent melting seasons. The upper snow and firn layers of the dry snow facies and percolation facies were also saturated with relatively large volumetric fractions of meltwater as compared to the negligible to limited volumetric fractions of meltwater that percolates during more typical seasonal surface melting on the GrIS. Seasonal meltwater was refrozen into spatially coherent melt layers following the 2010 and 2012 melting seasons (Culberg et al., 2021) as well as following the 2015 and 2018 melting seasons (i.e., identified as part of the temporal L-band signature analysis in this study; see Section 2.4.2).

As compared to ice slabs, which are dense low-permeability solid-ice layers, spatially coherent melt layers are a network of embedded ice structures primarily consisting of discontinuous horizontally-oriented ice layers and ice lenses sparsely connected via vertical-oriented ice pipes (Culberg et al., 2021). Ice slabs are relatively thick (~1 m – 16 m) and form in the high-elevation percolation facies (~2100 m.a.s.l.) at depths of between ~1 m and 20 m beneath the ice sheet surface following intense seasonal surface melting over multiple melting seasons (McFerrin et al., 2019). Spatially coherent melt layers are relatively thin (~0.02 cm - 2 m) and can rapidly form across the entire high-elevation dry snow facies (~3200 m.a.s.l ; Nghiem et al., 2012) at depths of less than ~1 m beneath the ice sheet surface following a single extreme melting season. They can further merge together into thicker solid-ice layers following multiple extreme melting seasons (Culberg et al., 2021). Similar to ice slabs, the formation of spatially coherent melt layers reduces the pore space within the upper snow and firn layers and may also facilitate lateral meltwater flow with minimum vertical percolation into the deeper firn layers, thus enhancing meltwater run-off from significantly higher elevations downslope towards the periphery on accelerated time scales. The formation of spatially coherent melt layers overlying deeper perennial firn aquifers (e.g., Fig. 3a) will limit or terminate gravity-driven meltwater drainage and seasonal recharging (Fountain and Walder, 1998), which may eventually completely refreeze stored meltwater into decimeters thick solid-ice layers overlying deeper glacial ice. Spatially coherent melt layers are exceptionally bright in AR radargrams (e.g., Fig 3a). The large dielectric contrast between the spatially coherent melt layer and the overlying, underlying, and interior snow and firn layers results in high reflectivity at the interfaces. However, electromagnetic energy still propagates downward through the high reflectivity layer into the deeper firn layers. Culberg et al., 2021) recently demonstrated mapping the extent of the spatially coherent melt layer formed following the anomalous 2012 melting season (Nghiem et al., 2012) via AR (Figs. 1c; 2).

https://doi.org/10.5194/tc-2021-116
Preprint. Discussion started: 30 April 2021

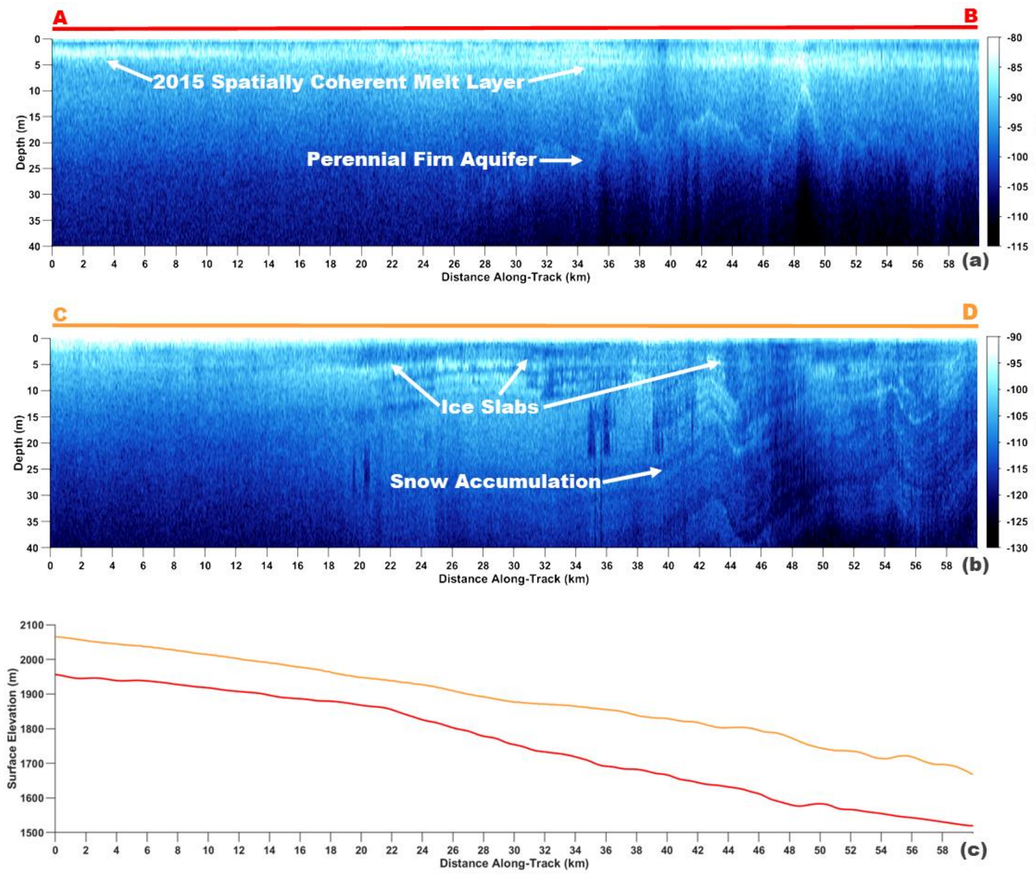

Figure 3

AR radargram profile (Rodriguez-Morales et al, 2014) (a) along perennial firn aquifer transect A-B (red line, Figs. 1; 2a) that was collected on 22 April 2017, and (b) ice slab transect C-D (orange line, Figs. 1; 2b) that was collected on 5 May 2017. (c) The corresponding perennial firn aquifer transect A-B elevation profile (red line), and ice slab transect C-D elevation profile (orange line). The exceptionally bright upper surface-parallel reflector in (a) is interpreted as a spatially coherent melt layer that formed following the 2015 melting season. The bright lower reflector in (a) is interpreted as the upper surface of meltwater stored within a perennial firn aquifer. Thick dark surface-parallel regions of low-reflectivity in (b) are interpreted as ice slabs. Alternating sequences of bright and dark surface-parallel reflectors in (b) are interpreted as seasonal snow accumulation layers. A first maximum after maximum gradient re-tracker is used to identify the surface return in each profile. Each profile is flattened so that the depth axis is measured relative to the local elevation. Corresponding elevation profiles in (c) are calculated by subtracting the radar-measured flight clearance over the ice sheet from the aircraft's global positioning system altitude measurements that were coincidently collected along each transect.

https://doi.org/10.5194/tc-2021-116
Preprint. Discussion started: 30 April 2021

AR and MCoRDS (Rodriguez-Morales et al, 2014) were flown over the GrIS on a P-3 aircraft in April and May between 2010 and 2017. The AR instrument operates at a center frequency of 750 MHz with a bandwidth of 300 MHz, resulting in a range resolution in firn of 0.53 m (Lewis et al., 2015). The collected data have an along-track resolution of ~30 m with 15 m spacing between traces in the final processed radargrams. At a nominal flight altitude of 500 m above the ice sheet surface, the cross-track resolution varies between 20 m for a smooth surface, to 54 m for a rough surface with no appreciable layover. The MCoRDS instrument operated at three different frequency configurations: (1) a center frequency of 195 MHz with a bandwidth of 30 MHz (2010-2014, 2017, 2018), (2) a center frequency of 315 MHz with a band width of 270 MHz (2015), and (3) a center frequency of 300 MHz with a bandwidth of 300 MHz (2016). The vertical range resolution in firn for each of these frequency configurations is 5.3 m, 0.59 m, and 0.53m, respectively (CReSIS, 2016). The collected data have an along-track resolution of ~25 m with 14 m spacing between traces in the final processed radargrams. At the same nominal flight altitude of 500 m, the cross-track resolution varies between 40 m for a smooth surface in the highest bandwidth configuration, to 175 m for a rough surface with no appreciable layover in the lowest bandwidth configuration.

The multi-year calibration technique uses perennial firn aquifer detections previously identified along OIB flight lines via AR (2010-2014) and MCoRDS (2015-2017) radargram profiles and the methodology described in Miège et al. (2016). Bright lower reflectors that undulate with the local topographic gradient underneath which reflectors are absent in the percolation facies are interpreted as the upper surface of meltwater stored within perennial firn aquifers (e.g., Fig. 3a). The large dielectric contrast between refrozen and water-saturated firn layers results in high reflectivity at the interface. However, the presence of meltwater increases attenuation, limiting the downward propagation of electromagnetic energy through the water-saturated firn layer. The total number of AR derived perennial firn aquifer detections is ~325,000, corresponding to a total extent of ~98 km^2. The analysis assumes a smooth surface, which is typical of much of the percolation facies, and a grid cell size of 15 m x 20 m. The total number of MCoRDS-derived perennial firn aquifer detections is ~142,000, corresponding to a total extent of ~80 km^2. This also assumes a smooth surface, and a grid cell size of 14 m x 40 m. The combined total number of grid cells (~467,000) and total extent (~178 km^2) is significantly larger than the total number of MCoRDS-derived grid cells (~78,000) and total extent (~44 km^2) calculated for 2016 (Miller et al., 2020). Perennial firn aquifer detections are mapped in western, southern, and south and central eastern Greenland as well as the Maniitsoq and Flade Isblink Ice Caps (Figs. 1c; 2a). We project AR- and MCoRDS-derived perennial firn aquifer detections on the NH EASE-Grid 2.0 at an rSIR grid cell spacing of 3.125 km. Each rSIR grid cell has an extent of ~10 km^2. The total number of rSIR grid cells with at least one perennial firn aquifer detection is ~800, corresponding to a total extent of ~8000 km^2. However, given the limited AR and MCoRDS grid cell coverage, less than ~1% of the rSIR grid cell extent has radargram coverage. As compared to the total number of MCoRDS-derived perennial firn aquifer detections (~780) calculated for 2016 (Miller et al., 2020), the total number of rSIR grid cells with at least one detection is only increased by ~20 for the multi-year calibration technique, corresponding to an increased total extent of ~200 km^2.

https://doi.org/10.5194/tc-2021-116
Preprint. Discussion started: 30 April 2021

We also use ice slab detections previously identified along OIB flight lines via AR (2010-2014) radargram profiles and the methodology described in McFerrin et al. (2019) in the multi-year calibration technique. Thick dark surface-parallel regions of low-reflectivity in the percolation facies are interpreted as ice slabs (Fig. 3b). The large dielectric contrast between ice slabs and the overlying and underlying snow and firn layers results in high reflectivity at the interfaces. However, electromagnetic energy is not scattered or absorbed within the homogeneous ice slab, it instead propagates downward through the layer and into the deeper firn layers. The total number of AR-derived ice slab detections is ~505,000, corresponding to a total extent of ~283 km^2. Ice slab detections are mapped in western, central and north eastern, and northern Greenland as well as the Flade Isblink Ice Cap (Figs. 1c; 2b). We project the AR-derived ice slab detections on the NH EASE-Grid 2.0 at an rSIR grid cell spacing of 3.125 km. The total number of rSIR grid cells with at least one ice slab detection is ~2000, corresponding to a total extent of ~20,000 km^2.However, less than ~2% of the rSIR grid cell extent has radargram coverage.

We detect perched firn aquifer areas by comparing the AR- and MCoRDS-derived perennial firn aquifer and ice slab detections projected on the NH EASE-Grid 2.0 and then identify overlapping rSIR grid cells. The total number of AR-derived perched firn aquifer detections is ~75,000, corresponding to a total extent of ~23 km^2. The total number of MCoRDS-derived perched firn aquifer detections is ~20, corresponding to a near-negligible extent (~0.006 km^2). Perched firn aquifer detections are mapped in western, and central eastern Greenland as well as the Flade Isblink Ice Cap (Figs. 1c; 2b).

The total number of rSIR grid cells with at least one perched firn aquifer detection is ~200, corresponding to a total extent of ~2000 km^2. However, similar to the other sub-facies, less than ~1% of the rSIR grid cell extent has radargram coverage. The total number of AR- and MCoRDS-derived perennial firn aquifer, ice slab, and perched firn aquifer detections that we project on three separate NH EASE-Grids 2.0, the associated total number of rSIR grid cells that we use in the calibration of our adapted empirical algorithm, and the coverage of detections and rSIR grid cells over each of the three sub-facies within the broader percolation facies are summarized in Table 1.

Table 1. *The total number of airborne ice penetrating radar survey detections (2010-2017), the associated total number of rSIR grid cells, and the coverage of detections and rSIR grid cells over perennial firn aquifer, ice slab, and perched firn aquifer areas.*

	Detections	Coverage (km^2)	rSIR Grid Cells	Coverage (km^2)
Perennial Firn Aquifers	~467,000	~178	~80	~8000
Ice Slabs	~505,000	~283	~2000	~20,000
Perched Firn Aquifers	~75,000	~23	~200	~2000

https://doi.org/10.5194/tc-2021-116
Preprint. Discussion started: 30 April 2021

2.4 Empirical Algorithm

2.4.1 Greenland's Ice Facies

Greenland's ice facies (i.e., dry snow facies - percolation facies - wet snow facies - ablation facies) were first described in detail by Benson et al., (1960), and were shown to represent the GrIS's response to climate. Evolution of the boundaries of Greenland's ice facies are often used as an indicator of climate change. Early studies using field-based (Jezek et al., 1994; Zabel et al., 1995), airborne (Swift et al., 1985; Bindschadler et al., 1987; Rignot et al., 1993; Jezek et al., 1993), and satellite (Fahnestock et al., 1993; Long and Drinkwater, 1994; Parrington, 1998) synthetic aperture radars and radar scatterometers operating at frequencies between Ku-band (13 GHz) and P-band (0.4 GHz) have demonstrated the exceptional capabilities of microwave sensors for mapping Greenland's ice facies. Early airborne studies using C-band microwave radiometry (Swift et al., 1985), and more recent studies using L-band microwave radiometry (Jezek et al. 2018) have demonstrated similar capabilities. In this study, we extend these capabilities to include satellite L-band microwave radiometry. We delineate the boundaries of the percolation facies relative to the adjacent dry snow facies (i.e., where negligible seasonal surface melting occurs) and wet snow facies (i.e., where snow layers are fully water-saturated during the melting season and subsequently refreeze as superimposed ice overlying deeper glacial ice). And, we further identify sub-facies (i.e., perennial firn aquifer, ice slabs, and perched firn aquifers) within the broader percolation facies that are currently experiencing rapid expansion (McFerrin et al., 2019; Culberg et al., 2021) as Greenland's climate continues to warm (Hanna et al., 2013; Cullather et al., 2020) and seasonal surface melting increases in extent, intensity, and duration (Steffen et al., 2004; Tedesco e al., 2008; Tedesco et al., 2011; Nghiem et al., 2012; Tedesco et al., 2016; Tedesco and Fettweis, 2020; Tedesco and Fettweis, 2020). Higher frequency microwave sensors provide shallower penetration depths, and an increased sensitivity to snow grain size, layering, embedded ice structures (Long and Drinkwater, 1994; Drinkwater et al., 2001) and stored meltwater (Jezek et al., 1993; Miller, 2019) within the upper snow and firn layers of the percolation facies. Lower frequencies provide deeper penetration depths and a range of sensitivities to embedded ice structures (Jezek et al., 1993; Jezek et al., 2018) and stored meltwater (Miller et al., 2020) in the deeper firn layers.

2.4.2 Temporal L-band signatures over the percolation facies

Microwave brightness temperature (T^B) expresses the satellite-observed magnitude of thermal emission and is influenced by the observation geometry as well as the dielectric and geophysical properties of the ice sheet (Ulaby et al., 2014). The most significant geophysical property influencing T^B is the volumetric fraction of meltwater within the snow and firn pore space (Mätzler and Hüppi, 1989). During the melting season, the upper snow and firn layers of the percolation facies are saturated with large volumetric fractions of meltwater that percolates vertically into the deeper firn layers (Benson, 1960; Humphrey et al., 2012). Increases in the volumetric fraction of meltwater results in rapid relative increases in the imaginary part of

https://doi.org/10.5194/tc-2021-116
Preprint. Discussion started: 30 April 2021

the complex dielectric constant (Tiuiri et al., 1984), with corresponding increases in T^B. This increase is attributed to a decrease in volume scattering, and penetration depth. The L-band penetration depth can rapidly decrease from ~tens to hundreds of meters, to less than ~a meter, dependent on the local snow and firn conditions, and englacial firn hydrological features. Surface and subsurface water-saturated snow and firn layers and embedded ice structures subsequently refreeze. During the freezing season, decreases in the volumetric fraction of meltwater results in rapid relative decreases in the imaginary part of the complex dielectric constant, with corresponding decreases in T^B. This increase is attributed to an increase in volume scattering, and penetration depth. The L-band penetration depth increases back to ~tens to hundreds of meters on variable time scales.

We analyze melting and freezing seasons in temporal L-band signatures exhibited in T_V^B time series (1 April 2015 - 31 March 2019) over and near AR- and MCoRDS-derived perennial firn aquifer, ice slab, and perched firn aquifer detections projected on NH EASE-Grids 2.0 (Fig. 4). We project ice surface temperature data calculated using thermal infrared brightness temperature collected by the Moderate Resolution Imaging Spectroradiometer (MODIS) on the Terra and Aqua satellites (i.e., Hall et al., 2012) on coincident NH EASE-Grids 2.0 at a 3.125 km rSIR grid cell spacing. We then derive melt onset and surface freeze-up dates (2015-2019) for each rSIR grid cell using the methodology described in Miller et al., (2020). We set a threshold of ice surface temperature >−1°C for meltwater detection (Nghiem et al., 2012), consistent with the ±1°C accuracy of the ice surface temperature data. For temperatures that are close to 0°C, ice surface temperatures are closely compatible with contemporaneous NOAA near-surface air temperature data (Shuman et al., 2014). Melt onset and surface freeze-up dates are overlaid on T_V^B time series to partition the melting and freezing seasons. Melt onset dates occur between ~April and July, and surface freeze-up dates occur between ~July and September. The melting season increases in duration moving downslope from the dry snow facies, and ranges from a single day in the highest elevations (>2500 m) of the percolation facies, to ~150 days in the ablation facies. Similarly, the associated freezing season decreases in duration moving downslope and ranges from between ~215 days and 365 days.

Over perennial firn aquifer areas (e.g., Figs. 1c; 2a; 4a), T_V^B is radiometrically warm during the melting season. Vertically percolating meltwater and gravity-driven meltwater drainage seasonally recharges perennial aquifers at depth (Fountain and Walder et al., 1998). Maximum values range from between ~200 K and 275 K during seasonal surface melting. Temporal L-band signatures exhibit increases on time scales of ~days to weeks following the melt onset date, and melting seasons range from between ~75 and 100 days. T_V^B remains radiometrically warm during the freezing season as a result of latent heat continuously released by the slow refreezing of the deeper firn layers that are saturated with large volumetric fractions of meltwater (Miller et al, 2020). Minimum values range from between ~180 K and 250 K following the surface freeze-up date. L-band emissions from the radiometrically warm upper snow and firn layers decrease during the freezing season as embedded ice structures slowly refreeze at increased depths below the ice sheet surface (Miller et al., 2020). Temporal L-band signatures exhibit exponential decreases on time scales of ~months that approach and sometimes achieve relatively stable T_V^B values,

https://doi.org/10.5194/tc-2021-116
Preprint. Discussion started: 30 April 2021

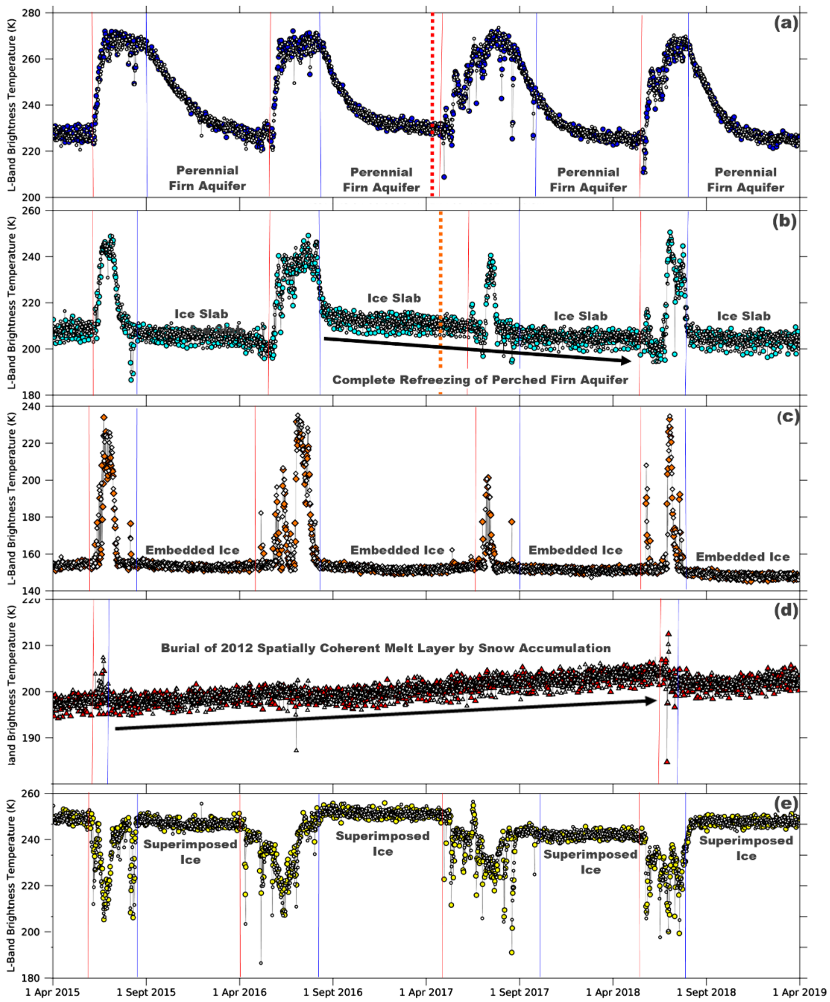

Figure 4

Temporal L-band signatures that alternate morning (white symbols) and evening (colored symbols) orbital pass interval enhanced-resolution T_V^B generated using observations collected over the GrIS by the microwave radiometer on the SMAP satellite (Brodzik et al., 2019) over (a) perennial firn aquifer area (blue circles; Figs. 2a; 3a), (b) perched firn aquifer area (cyan circles; Figs. 2b; 3b), (c) percolation facies area (orange diamonds; Fig 2b), (d) high-elevation (~2500 m.a.s.l.) spatially coherent melt layer area (red triangles; Fig. 2a), and (e) superimposed ice area (yellow circles; Fig. 2b). Melt onset (red lines) and surface freeze-up (blue lines) dates are derived from thermal infrared T^B collected by MODIS on the Terra and Aqua satellites (Hall et al, 2012). AR radargram profile along perennial firn aquifer transect A-B (red dashed line; Figs. 1; 2a; 3a) that was collected on 22 April 2017, and ice slab transect C-D (orange dashed line; Figs. 1; 2b; 3b) that was collected on 5 May 2017.

https://doi.org/10.5194/tc-2021-116
Preprint. Discussion started: 30 April 2021

and freezing seasons range from between ~265-290 days. T_V^B often decreases by more than ~50 K during the freezing season (e.g., Fig. 4a), representing the descent of the upper surface of stored meltwater by ~tens of meters (Miège et al., 2016).

Over ice slab and perched firn aquifer areas (e.g., Figs. 1c; 2b; 5b), T_V^B is typically radiometrically colder than over perennial firn aquifer areas during the melting season. The presence of dense low-permeability solid-ice layers (e.g., Fig. 3b) reduces the snow and firn pore space available to store seasonal meltwater at depth. Meltwater may alternatively run-off downslope towards the wet snow facies. Maximum values range from between ~170 K and 260 K during seasonal surface melting. Temporal L-band signatures exhibit increases on time scales of ~days to weeks following the melt onset date, and melting seasons range from between ~60 and 90 days. T_V^B is also typically radiometrically colder than over perennial firn aquifer areas during the freezing season as a result of the absence of meltwater stored at depth (i.e. ice slab areas), or the presence of limited volumetric fractions of meltwater stored at depth in shallow water-saturated firn layers (i.e. perched firn aquifer areas). Minimum values range from between ~130 K and 240 K following the surface freeze-up date. Temporal L-band signatures exhibit exponential decreases on time scales of ~weeks to months that often achieve relatively stable T_V^B values, and freezing seasons range from between ~275-305 days. Exponentially decreasing temporal L-band signatures sometimes transition to linearly decreasing on time scales of ~years following the surface freeze-up date (e.g., between ~September 2016 and May 2018 in Fig. 4b). We infer this indicates the formation and subsequent refreezing of a shallow perched firn aquifer on top of a buried ice slab or other semi-impermeable layer. As compared to the large T_V^B decreases in percolation facies areas, T_V^B decreases over perched firn aquifer areas are as small as ~a few K annually, which represents the descent of the upper surface of stored meltwater by ~meters rather than by ~tens of meters.

Over other percolation facies areas, where seasonal meltwater is fully refrozen and stored exclusively as embedded ice (e.g., Fig. 4c), T_V^B is typically radiometrically colder than over perennial firn aquifer, ice slab, and perched firn aquifer areas during the melting season. Maximum values range from between ~150 K and 200 K during seasonal surface melting. Temporal L-band signatures exhibit increases on time scales of ~days to weeks following the melt onset date, and melting seasons range from between ~1 and 60 days. T_V^B is also typically radiometrically cold during the freezing season. Minimum values range from between ~130 K and 180 K following the surface freeze-up date. Temporal L-band signatures exhibit exponential decreases on time scales of ~days to weeks and achieve relatively stable T_V^B values, and freezing seasons range from between ~305-364 days. However, over the highest elevations (> ~2500 m.a.s.l.) of the percolation facies approaching the dry snow line, where seasonal surface melting and the formation of embedded ice structures is limited, T_V^B remains radiometrically warm during the freezing season. Minimum values range from between ~180 K and 220 K following the surface freeze-up date. We infer T_V^B decreases, sometimes step-responses exceeding ~10 K, that follow the surface freeze-up date (e.g., between April 2018 and September 2018 in Fig. 4c) are a result of an increase in volume scattering from newly formed embedded ice structures within a spatially coherent melt layer. We also infer that temporal L-band signatures that increase several K on time scales of ~years (e.g., between ~April 2015 and April 2018 in Fig. 4c) indicate the burial of spatially coherent melt layers formed following the 2010, 2012, 2015, and 2018 melting seasons by snow accumulation.

Exponentially decreasing temporal L-band signatures transition smoothly between perennial firn aquifer, ice slab, perched firn aquifer, and other percolation facies areas – there are no distinct temporal L-band signatures that delineate boundaries between these sub-facies. Boundary transitions between other facies, however, are delineated both above and below the percolation facies. Over the dry snow facies (e.g., Fig. 4d), T_V^B is radiometrically warm during the melting and freezing seasons. Values range from between ~200 K and 240 K. While T_V^B is known to be relatively stable in the dry snow facies, temporal L-band signatures that increase on time scales of ~years are observed throughout this region at elevations as high as Summit Station (~3200 m.a.s.l), similar to those observed in the highest elevations (> ~2500 m.a.s.l.) of the percolation facies. We infer increasing temporal L-band signatures indicate the burial of the spatially coherent melt layer formed following the anomalous 2012 melting season (Nghiem et al., 2012) by snow accumulation (Culberg et al., 2021). Over the wet snow facies (e.g., Fig. 4e), where seasonal meltwater is fully refrozen and stored as superimposed ice, T_V^B is radiometrically warm during the melting season. Maximum values range from between ~230 K and 250 K during seasonal surface melting. As compared to the percolation facies, where temporal L-band signatures exhibit rapid increases following melt onset, temporal L-band signatures reverse and exhibit decreases on time scales of ~days to weeks, and melting seasons that range between ~90-120 days. We infer these reversals are the result of high reflectivity and attenuation at the fully water-saturated snow layer and/or at the wet, rough superimposed ice-air interface. Meltwater runs-off superimposed ice downslope towards the ablation facies in the wet snow facies. T_V^B remains radiometrically warm during the freezing season. Minimum values range from between ~230 K and 250 K following seasonal surface melting. Temporal L-band signatures exhibit increases on time scales of ~days that achieve relatively stable T_V^B values, and freezing seasons range from between ~245 and 275 days.

The MODIS-derived total number of days in the melting and freezing seasons estimated from melt onset and surface freeze-up dates, the SMAP-derived maximum and minimum vertically-polarized L-band brightness temperature, and the time scales of exponential decrease following the surface freeze-up date estimated for each T_V^B time series for rSIR grid cells over perennial firn aquifer, ice slab, perched firn aquifer, and other percolation facies areas as well as for the dry snow facies, and the wet snow facies are summarized in Table 2.

https://doi.org/10.5194/tc-2021-116
Preprint. Discussion started: 30 April 2021

Table 2. *The MODIS-derived total number of days in the melting and freezing seasons (2015-2019), the SMAP-derived maximum vertically-polarized L-band brightness temperature ($T^B_{V,max}$), the minimum vertically-polarized L-band brightness temperature ($T^B_{V,min}$), and the time scale scales of exponential decrease following the surface freeze-up date (1 April 2015 - 31 March 2019) for perennial firn aquifer, ice slab, perched firn aquifer, and other percolation facies areas as well as for the dry snow facies and the wet snow facies.*

	Melting Season (days)	Freezing Season (days)	$T^B_{V,max}$ (K)	$T^B_{V,min}$ (K)	Exponential Decrease (time scale)
Perennial Firn Aquifers	~75 - 100	~265 - 290	~200 - 275	~180 – 250	~weeks – months
Ice Slabs / Perched Firn Aquifers	~60 -90	~275 - 305	~170 - 260	~130 – 240	~days - Weeks
Percolation Facies	~1 - 60	~305 - 364	~150 - 200	~130 – 220	~days
Dry Snow Facies	-	365	~200 - 240	~200 – 240	-
Wet Snow Facies	~90 - 120	~245 - 275	~230 - 250	~230 – 250	-

2.4.3 L-band geophysical-brightness temperature model

Based on our analysis of $T^B_{V,max}$ and $T^B_{V,min}$ values in temporal L-band signatures over the percolation facies, we derive a 'firn saturation' parameter using the simple two-layer L-band geophysical-brightness temperature model described in Ashcraft and Long (2006). The firn saturation parameter is similar to the 'melt intensity' parameter derived in Hicks and Long (2011) that uses enhanced resolution vertically-polarized Ku-band radar backscatter imagery (2003) collected by the SeaWinds radar scatterometer that was flown in tandem on NASA's Quick SCATterometer (QuikSCAT) satellite (Tsai et al., 2000) and JAXA's Advanced Earth Observing Satellite 2 (ADEOS-II) (Freilich et al., 1994). We use the firn saturation parameter to estimate the maximum seasonal volumetric fraction of meltwater within the saturated upper snow and firn layers of the percolation facies using $T^B_{V,max}$ and $T^B_{V,min}$values extracted from T^B_V time series (1 April 2015 - 31 March 2019). We calculate the firn saturation parameter for each rSIR grid cell within the ice sheet-masked extent of the GrIS as part of our adapted empirical algorithm (see Section 2.4.5).

We first describe the geophysical model as follows. We assume a base layer underlying a water-saturated firn layer with a given depth and volumetric fraction of meltwater. Each of the layers is homogenous. We next describe T^B_V from the geophysical model (Eq. 1). The ice sheet is discretely layered (i.e., two-layers; the base layer, and the water-saturated firn layer) to calculate T^B_V at an oblique incidence angle. Emissions from the base layer are a function of both the macroscopic roughness and the dielectric properties of the layer. They occur in conjunction with volume scattering at depth, and are locally dependent

https://doi.org/10.5194/tc-2021-116
Preprint. Discussion started: 30 April 2021

on englacial firn hydrological features, including embedded ice structures, spatially coherent melt layers, ice slabs, and perennial and perched firn aquifers. Reflectivity at depth (i.e., at the base layer-water-saturated firn layer interface), and at the ice sheet surface (i.e., at the water-saturated firn layer-air interface) is neglected. The contribution from each layer is individually calculated.

The two-layer L-band geophysical-brightness temperature model is represented analytically by

$$T_{V,max}^{B} = T\left(1 - e^{-\kappa_e d sec\theta}\right) + T_{V,min}^{B} e^{-\kappa_e d sec\theta} \ , \qquad \text{(Eq. 1)}$$

where $T_{V,max}^{B}$ is the maximum vertically-polarized L-band brightness temperature at the ice sheet surface, $T_{V,min}^{B}$ is the minimum vertically-polarized L-band brightness temperature emitted from the base layer, T is the physical temperature of the water-saturated firn layer, θ is the transmission angle, κ_e is the extinction coefficient, and d is depth.

We invert Eq. 1 and solve for the firn saturation parameter (ξ)

$$\xi = l\,n\left(\frac{T_{V,max}^{B} - T}{T_{V,min}^{B} - T}\right) cos\theta \ , \qquad \text{(Eq. 2)}$$

where $\xi = \kappa_e d$. The maximum vertically-polarized L-band brightness temperature asymptotically approaches the physical temperature of the water-saturated firn layer as the extinction coefficient and the depth of the water-saturated firn layer increases. The extinction coefficient is defined as the sum of the Raleigh scattering coefficient (κ_s) and the absorption coefficient (κ_a). For water-saturated firn, absorption dominates over scattering, and increases in the extinction coefficient are controlled by the volumetric fraction of meltwater (m_v). We assume that thicker water-saturated firn layers with larger volumetric fractions of meltwater generate higher firn saturation parameter values. However, the thickness of the water-saturated firn layer is limited by the L-band penetration depth. Theoretical L-band penetration depths calculated for a water-saturated firn layer range from between ~10 m for small volumetric fractions of meltwater (m_v<1%), and ~1 cm for large volumetric fractions of meltwater (m_v=20%) (Fig. 5). Large volumetric fractions of meltwater results in high reflectivity and attenuation at the interface between water-saturated firn layers and the overlying refrozen firn layers, and between glacial ice or a semi-impermeable layer and the overlying water-saturated firn layers, and a radiometrically cold firn layer (e.g., Fig 5e).

https://doi.org/10.5194/tc-2021-116
Preprint. Discussion started: 30 April 2021

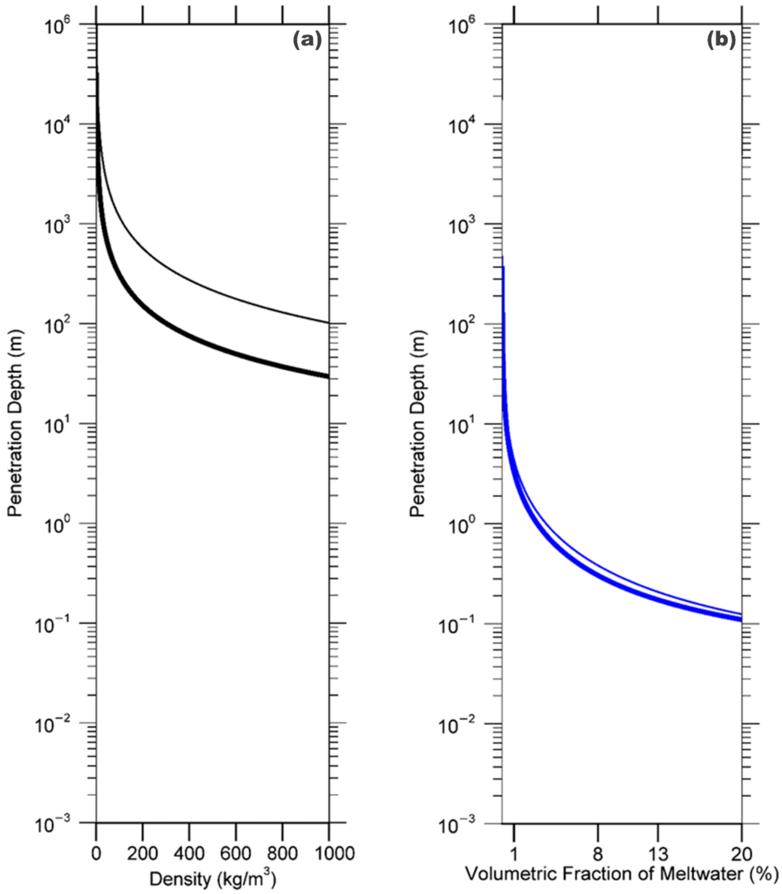

Figure 5

Theoretical L-band penetration depths for (a) refrozen, and (b) water-saturated firn. Penetration depths $\left(\frac{1}{\kappa_s+\kappa_a}\right)$ are calculated as a function of the Raleigh scattering coefficient (κ_s; Eq. 8) and the absorption coefficient (κ_a; Eq. 10), which are functions of the dielectric and geophysical properties of the GrIS. The complex dielectric constant is calculated using the empirically derived models described in Tiuri et al., (1984). Refrozen firn penetration depths are calculated as a function of firn density (ρ_{firn}), and the curves are plotted for snow grain radii (r) set to r =0.5 mm (upper curve), and r =4 mm (lower curve). Water-saturated firn penetration depths are calculated as a function of the volumetric fraction of meltwater (m_v), and the curves are plotted for firn density set to ρ_{firn}=400 kg/m^3 (upper curve), and ρ_{firn}=917 kg/m^3 (lower curve). Given the complexity of modeling embedded ice structures, they are excluded from the penetration depth calculation. Increases in the volumetric fraction of embedded ice in the firn will result in an increase in volume scattering, which will decrease and compress the distance between the penetration depth curves for both refrozen and water-saturated firn.

https://doi.org/10.5194/tc-2021-116
Preprint. Discussion started: 30 April 2021

2.4.4 Continuous logistic model

We adapt our previously developed empirical algorithm to map the extent of Greenland's perennial firn aquifers (Miller et al., 2020) to also map the extent of ice slab and perched firn aquifer areas. The empirical algorithm is derived from the continuous logistic model, which is based on a differential equation that models the decrease in physical systems as a function of time using a set of sigmoidal curves. These curves begin at a maximum value with an initial interval of decrease that is approximately exponential. Then, as the function approaches its minimum value, the decrease slows to approximately linear. Finally, as the function asymptotically reaches its minimum value, the decrease exponentially tails off and achieves stable values. We use the continuous logistic model to parametrize the refreezing rate within the saturated upper snow and firn layers of the percolation facies using T_V^B time series (1 April 2015 - 31 March 2019) that are partitioned using $T_{V,max}^B$ and $T_{V,min}^B$ values. We calculate the refreezing rate for each rSIR grid cell within the percolation facies extent as part of our adapted empirical algorithm (see Section 2.4.5).

The continuous logistic model is described by a differential equation known as the logistic equation

$$\frac{dx}{dt} = \zeta x(1 - x) \quad \text{(Eq. 3)}$$

that has the solution

$$x(t) = \frac{1}{1+\left(\frac{1}{x_o}-1\right)e^{-\zeta t}}, \quad \text{(Eq. 4)}$$

where x_o is the function's initial value, ζ is the function's exponential rate of decrease, and t is time. The function $x(t)$ is also known as the sigmoid function. We use the sigmoid function to model the exponentially decreasing temporal L-band signatures observed over the percolation facies as a set of decreasing sigmoidal curves.

We first normalize T_V^B time series for each rSIR grid cell

$$T_{V,N}^B(t) = \frac{T_V^B(t)-T_{V,min}^B}{T_{V,max}^B-T_{V,min}^B}, \quad \text{(Eq. 5)}$$

where $T_{V,min}^B$ is the minimum vertically-polarized L-band brightness temperature, and $T_{V,max}^B$ is the maximum vertically-polarized L-band brightness temperature. We then apply the sigmoid fit

$$T_{V,N}^B\left(t \in \left[t_{max}, t_{min}\right]\right) = \frac{1}{1+\left(\frac{1}{T_{V,N}^B(t_{max})}-1\right)e^{-\zeta t}}. \quad \text{(Eq. 6)}$$

https://doi.org/10.5194/tc-2021-116
Preprint. Discussion started: 30 April 2021

$T_{V,N}^{B}\left(t \in [t_{max}, t_{min}]\right)$ is the normalized vertically-polarized L-band brightness temperature on the time interval $t \in [t_{max}, t_{min}]$, where t_{max} is the time the function achieves a maximum value, and t_{min} is the time the function achieves a minimum value. The initial normalized vertically-polarized L-band brightness temperature ($T_{V,N}^{B}(t_{max})$) is the function's maximum value. The final normalized vertically-polarized L-band brightness temperature ($T_{V,N}^{B}(t_{min})$) is the function's minimum value. The function's exponential rate of decrease represents the refreezing rate parameter (ζ). An example set of simulated sigmoidal curves is shown in Fig. 6.

2.4.5 SMAP-derived perennial firn aquifer, ice slab, and perched firn aquifer maps

Our adapted empirical algorithm uses ice sheet-masked SMAP enhanced-resolution T_V^B imagery over the GrIS that alternates morning and evening orbital pass observations annually, beginning and ending just prior to melt onset. Our algorithm is implemented in two steps: (1) mapping the extent of the percolation facies using the firn saturation parameter derived from the L-band geophysical-brightness temperature model (see Section 2.4.3), and (2) mapping the extent of perennial firn aquifer, ice slab, and perched firn aquifer areas over the percolation facies using the continuous logistic model (see Section 2.4.4) we calibrate using airborne ice-penetrating radar detections projected on three separate NH EASE-Grids 2.0 (see Section 2.2).

Using Eq. 2, we first set a threshold for the firn saturation parameter (ξ_T) defined by the relationship

$$\xi_T = (\kappa_s + \kappa_a)d \leq \xi \ . \qquad \text{(Eq. 7)}$$

We calculate the Raleigh scattering coefficient (κ_s) in Eq. 7 using

$$\kappa_s = N_d \frac{8}{3} k_o^4 r^6 \left|\frac{\varepsilon_r - 1}{\varepsilon_r + 2}\right|^2 , \qquad \text{(Eq. 8)}$$

where N_d is the particle density, k_o is the wave number of the background medium of air, r is the snow grain radius set to r=2 mm, and ε_r is the complex dielectric constant. The particle density is defined by

$$N_d = \frac{\rho_{firn}}{\rho_{ice}} \frac{1}{\frac{4}{3}\pi r^3} , \qquad \text{(Eq. 9)}$$

where ρ_{firn} is firn density, which we set to ρ_{firn}=400 kg/m^3, and ρ_{ice} is ice density, which we set to ρ_{ice}=917 kg/m^3. Our grain radius and firn density estimates are consistent with measurements within the upper snow and firn layers of the percolation facies of south eastern Greenland at the Helheim Glacier field site (Fig.

https://doi.org/10.5194/tc-2021-116
Preprint. Discussion started: 30 April 2021

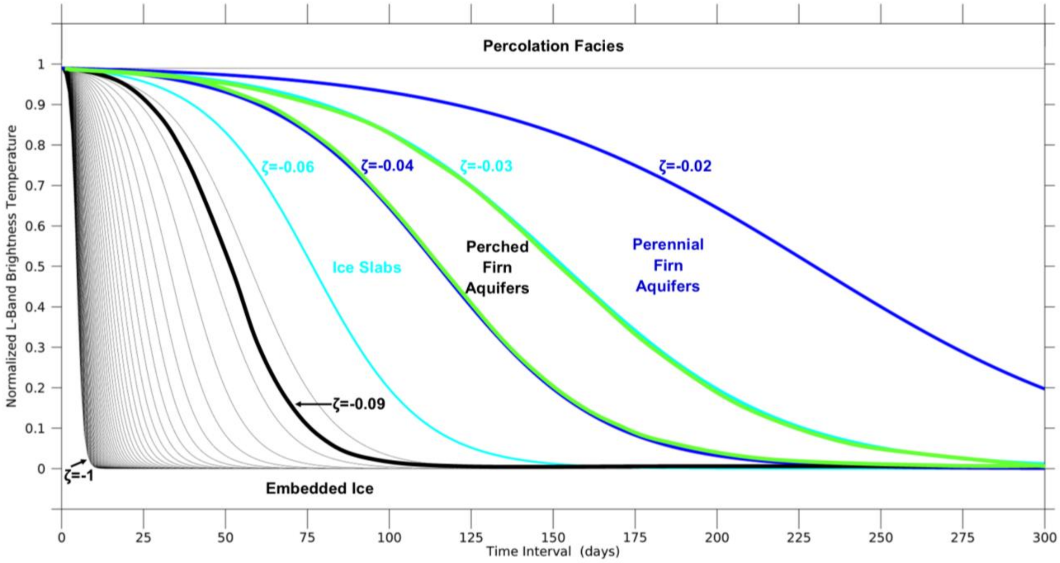

Figure 6

Example set of simulated sigmoidal curves that represent our model of the exponentially decreasing temporal L-band signatures predicted over the percolation facies. The initial normalized vertically-polarized L-band brightness temperature was fixed at a value of $T^B_{V,N}(t_{max})$ = 0.99, and the time interval was set to a value of $t \in \left[t_{max}, t_{min} \right]$ = 300 observations. The refreezing rate parameter was set to values between ζ = [-1, 0] incremented by steps of 0.02. The blue lines correspond to the interval $\zeta \in$ [-0.04, -0.02] and produce curves similar to those observed over perennial firn aquifer areas. The cyan lines correspond to the interval $\zeta \in$ [-0.06, -0.03] and produce curves similar to those observed over ice slab areas. The green lines correspond to the interval $\zeta \in$ [-0.04 ,-0.03] and produce curves similar to those observed over perched firn aquifer areas. The black line is the observed lower bound (ζ = -0.09) of the refreezing rate parameter of partitioned T^B_V time series (1 April 2015 - 31 March 2019) iteratively fit to the sigmoid function (see Section 3).

https://doi.org/10.5194/tc-2021-116
Preprint. Discussion started: 30 April 2021

2a; blue circle; Fig. 4a), where in situ perennial firn aquifer measurements have recently been collected (Miller et al., 2017).

We calculate the absorption coefficient (κ_a) in Eq. 7 using

$$\kappa_a = -2k_o\Im\{\sqrt{\varepsilon_r}\}\ , \qquad \text{(Eq. 10)}$$

where $\Im\{\ \}$ represents the imaginary part. We calculate the complex dielectric constant of the saturated firn layer in Eq. 8 and Eq. 10 using the empirically derived models described in Tiuri et al., (1984). We set the volumetric fraction of meltwater to m_v=1%. We set the depth of the water-saturated firn layer in Eq. 7 to d=1 m. These values are consistent with typical lower frequency (e.g., 37 GHz, 13.4 GHz, 19 GHz) passive (e.g., Mote, et al. 1995; Abdalati and Steffen, 1997; Ashcraft and Long, 2006) and active (e.g., Hicks and Long, 2011) microwave algorithms used to detect seasonal surface melting over the GrIS. Using the results of Eq. 7, 8, 9, and 10, we calculate the firn saturation parameter threshold at ξ_T=0.1.

The first step in our adapted empirical algorithm is to map the extent of the percolation facies. For each rSIR grid cell within the ice sheet-masked extent of the GrIS, we smooth the corresponding T_V^B time series (1 April 2015 - 31 March 2019) using a 14-observation (1 week) moving window. We extract the minimum vertically-polarized L-band brightness temperature ($T_{V,min}^B$), and the maximum vertically-polarized L-band brightness temperature ($T_{V,max}^B$). We set the physical temperature of the water-saturated firn layer to T=273.15 K, and the transmission angle to θ=40°. We then calculate the firn saturation parameter (ξ) using Eq. 2. If the calculated firn saturation parameter exceeds the firn saturation parameter threshold, the rSIR grid cell is converted to a binary parameter to map the total extent of the percolation facies.

We note that smoothing T_V^B time series will mask brief low-intensity seasonal surface melting that occurs in the high-elevation (> ~2500 m) percolation facies, where seasonal meltwater is rapidly refrozen within the colder snow and firn layers (e.g., Fig. 4d). Thus, the calculated firn saturated parameter will not exceed the firn saturation parameter threshold, and these rSIR grid cells will be excluded from the algorithm. The exclusion of rSIR grid cells in the high-elevation percolation facies is not expected to have a significant impact on our results as our algorithm targets rSIR grid cells in areas that experience intense seasonal surface melting. The exclusion of rSIR grid cells will, however, slightly underestimate the mapped percolation facies extent.

The second step in our adapted empirical algorithm is to map the extent of perennial firn aquifer, ice slab, and perched firn aquifer areas over the percolation facies. For each rSIR grid cell within the mapped percolation facies extent, we normalize the corresponding T_V^B time series (1 April 2015 - 31 March 2019) using Eq. 5 ($T_{V,N}^B(t)$). We then extract the initial normalized vertically-polarized L-band brightness temperature, ($T_{V,N}^B(t_{max})$) and the final normalized vertically-polarized L-band brightness temperature ($T_{V,N}^B(t_{min})$), and partition $T_{V,N}^B(t)$ on the time interval $t \in [t_{max}, t_{min}]$. We smooth $T_{V,N}^B(t \in [t_{max}, t_{min}])$ using a 56-observation (4 week) moving window. The sigmoid fit is then iteratively applied using Eq. 6.

https://doi.org/10.5194/tc-2021-116
Preprint. Discussion started: 30 April 2021

Smoothing reduces the chi-squared error statistic when fitting $T^B_{V,N}(t \in [t_{max}, t_{min}])$ to the sigmoid function. We fix the initial normalized vertically-polarized L-band brightness temperature at $T^B_{V,N}(t_{max})$=0.99, which provides a uniform parameter space in which the refreezing rate parameter (ζ) can be analyzed. Variability in $T^B_{V,N}(t_{max})$ is controlled by the volumetric fraction of meltwater within the upper snow and firn layers of the percolation facies, and is accounted for in the firn saturation parameter (ξ), which is analyzed separately. $T^B_{V,N}(t \in [t_{max}, t_{min}])$ iteratively fit to the sigmoid function converge quickly (i.e., algorithm iterations I ∈ [5, 15]), and observations are a good fit (i.e., chi squared error statistic is $\chi 2 \in [0, 0.1]$).

Using the SMAP-derived $T^B_{V,N}(t_{max})$ and $T^B_{V,N}(t_{min})$, rather than the MODIS-derived initial normalized vertically-polarized L-band brightness temperature at the surface freeze-up date ($T^B_{V,N}(t_{sfu})$), and final normalized vertically-polarized L-band brightness temperature at the melt onset date ($T^B_{V,N}(t_{mo})$) that were used in the empirical algorithm described in Miller et al., 2020 (e.g., Fig. 4), has several advantages. They key advantage of this approach is that maps can be generated using T^B imagery collected from a single satellite, which simplifies the adapted empirical algorithm. Another advantage is that unlike T^B collected at shorter-wavelength thermal infrared frequencies (e.g., MODIS), T^B collected at longer wavelength microwave frequencies (e.g., SMAP) is not sensitive to clouds, which eliminates observational gaps and cloud contamination, and provides more accurate time series partitioning and more robust curve fitting. The mapped extent of Greenland's perennial firn aquifers generated by our adapted empirical algorithm and by our empirical algorithm (Miller et al., 2020) are consistent (see Section 3).

We calibrate our adapted empirical algorithm using the AR- and MCoRDS-derived perennial firn aquifer (2010-2017), ice slab (2010-2014), and perched firn aquifer (2010-2017) detections projected separately on three NH EASE-Grids 2.0. For each rSIR grid cell with at least one detection, we extract the corresponding maximum vertically-polarized L-band brightness temperature ($T^B_{V,max}$), the minimum vertically-polarized L-band brightness temperature ($T^B_{V,min}$), the firn saturation parameter (ξ), and the refreezing rate parameter (ζ), and for each of the extracted SMAP-derived calibration parameters we calculate the standard deviation (σ). Similar to Miller et al., 2020, thresholds of ±2σ are set for each of the extracted SMAP-derived calibration parameters in an attempt to eliminate peripheral rSIR grid cells near the ice sheet edge and near the upper and lower boundaries of each sub-facie, where L-band emissions can be influenced by morphological features, such as crevasses, superimposed and glacial ice, and spatially integrated with emissions from rock, land, the ocean, and adjacent percolation facies and wet snow facies areas. The SMAP-derived calibration parameter threshold intervals extracted from T^B_V time series that we use to map perennial firn aquifer, ice slab, and perched firn aquifer areas are given in Table 3. We apply the calibration to each rSIR grid cell within the percolation facies extent. If the extracted SMAP-derived calibration parameters are within the threshold intervals, the rSIR grid cell is converted to a binary parameter to map the total extent of each of these sub-facies.

https://doi.org/10.5194/tc-2021-116
Preprint. Discussion started: 30 April 2021

Table 3. *SMAP-derived calibration parameter threshold intervals (1 April 2015 - 31 March 2019) used for mapping perennial firn aquifer, ice slab, and perched firn aquifer areas.*

	ξ	$T^B_{V,max}$ (K)	$T^B_{V,min}$ (K)	ζ
Perennial Firn Aquifers	0.2 – 4	200 – 275	180 – 250	-0.04 - -0.02
Ice Slabs	0.1 – 2	170 – 260	130 – 240	-0.03 - -0.06
Perched Firn Aquifers	0.2 - 1.2	200 – 260	180 – 240	-0.03 - -0.04

Iteratively applying the sigmoid fit to $T^B_{V,N}(t \in [t_{max}, t_{min}])$ over perched firn aquifer areas is a source of uncertainty in our adapted empirical algorithm. While the continuous logistic model is reasonable for the majority of exponentially decreasing temporal L-band signatures over the percolation facies, it is not optimal for exponentially decreasing temporal L-band signatures that transition to linearly decreasing on time scales of ~years following the surface freeze-up date. Especially multi-year linearly decreasing temporal L-band signatures over areas where perching occurs following intense seasonal surface melting and shallow water-saturated firn layers persist throughout the following freezing season as well as throughout weaker seasonal surface melting the following melting season (e.g., between ~September 2016 and May 2018 in Fig. 4b). Although $T^B_{V,N}(t \in [t_{max}, t_{min}])$ over perched firn aquifer areas iteratively fit to the sigmoid function converge quickly (i.e., algorithm iterations $I \in$ [8, 15]), and observations appear to be a good fit (i.e., chi squared error statistic is $\chi2 \in$ [0.06, 0.1]), simulated sigmoidal curves often asymptotically approach $T^B_{V,min}$ too quickly, which underestimates the refreezing rate parameter (ζ) to values outside the SMAP-derived calibration parameter threshold intervals. Perched firn aquifer areas may alternatively be mapped as ice slab areas or percolation facies areas, which will underestimate or overestimate the mapped extent of each of these sub-facies.

Miller et al., 2020 cited significant uncertainty in the SMAP-derived perennial firn aquifer extent as a result of the lack of a distinct temporal L-band signature delineating the boundary between perennial firn aquifer areas and adjacent percolation facies areas. In this study, similar uncertainty exists in the SMAP-derived perennial firn aquifer, ice slab, and perched firn aquifer extents. This uncertainty could, at least in part, be a result of the rSIR algorithm. An rSIR grid cell corresponds to the weighted average of T^B_V over SMAP's antenna footprint (Long et al., 2020). The weighting is the grid cell's spatial response function (SRF), which is ~18 km (i.e. the effective resolution) in diameter. The SRF is centered on the rSIR grid cell. Since the effective resolution (i.e., size of the 3 dB contour of the SRF) is less than the rSIR grid cell spacing, rSIR grid cell SRF's overlap and the grid cells T^B_V values are not statistically independent. This uncertainty, however, could also have a geophysical basis, as it is unlikely that the boundaries between sub-facies (perennial firn aquifers, ice slabs, and perched firn aquifers) as well as between facies (percolation facies, dry snow facies, wet snow facies) are distinct. The thickness of the water-saturated firn layer or ice slab may thin and taper-off at the periphery, and sub-facies and facies may become spatially scattered and

https://doi.org/10.5194/tc-2021-116
Preprint. Discussion started: 30 April 2021

merge together. Over SMAP's ~18 km footprint, spatially integrated L-band emissions may also result in a smooth transition between temporal L-band signatures.

The limited extent (AR, 15 m x 20 m; MCoRDS, 14 m x 40 m) of the airborne ice-penetrating radar detections as compared to the rSIR grid cell extent (3.125 km x 3.125 km) and the effective resolution (~18 km) of the SMAP enhanced-resolution T_V^B imagery is also cited in Miller et al., 2020 as a source of uncertainty in the empirical algorithm. In this study, similar uncertainty exists in our adapted empirical algorithm. The total rSIR grid cell extent with radargram coverage is less than 2%, which means that ~98% of the total rSIR grid cell extent with radargram coverage, from which the SMAP-derived calibration parameter threshold intervals are extracted, is unknown. Calculating the total rSIR grid cell extent where detections are absent along OIB flight lines and statistically integrating this calculation into the multi-year calibration technique may help reduce the uncertainty, particularly the significant uncertainty in the interannual variability, which we have yet to resolve. A sensitivity analysis suggests that even small changes in any of the SMAP-derived calibration parameter threshold intervals (i.e., several K for $T_{V,min}^B$, and $T_{V,max}^B$, several tenths of a percentage point for ξ, and several hundredths of a percentage point for ζ) can result in variability in the mapped extents of hundreds of square kilometers, and boundary transitions between perennial firn aquifer, ice slab, and perched firn aquifer areas. Thus, the mapped extent of each of these sub-facies of the broader percolation facies should simply be considered an initial result demonstrating the potential of our adapted empirical algorithm for future work.

3. Results and Discussion

The SMAP-derived maximum vertically-polarized L-band brightness temperature values generated by our adapted empirical algorithm range from between $T_{V,max}^B$=150 K and 275 K, and the minimum vertically-polarized L-band brightness temperature values range from between $T_{V,min}^B$=130 K and 250. These values are consistent with the range of $T_{V,max}^B$ and $T_{V,min}^B$ values given in the temporal L-band signature analysis (Section 2.4.2; Table 2). Firn saturation parameter values range from between ξ=0.1 and 4.0. Refreezing rate parameter values range from between ζ=-0.09 and -0.01. The lower bound (ζ=-0.09) of the refreezing rate parameter observed over the percolation facies is significantly higher than the predicted lower bound (ζ=-1) in our example set of simulated sigmoidal curves (black line, Fig. 6).

The SMAP-derived perennial firn aquifer (blue shading), ice slab (cyan shading), perched firn aquifer (green shading), and percolation facies (purple shading) extents (2015-2019) generated by our adapted empirical algorithm are shown in Figs. 7a-9a, and are summarized in Table 4. The percolation facies extent (~5.8 x 10^5 km^2) generated by our adapted empirical algorithm is mapped at elevations between ~500 m.a.s.l. and 3500 m.a.s.l., and extends over ~32 % of the GrIS extent (~1.8 x 10^6 km^2). The perennial firn aquifer extent (64,000 km^2) is mapped at elevations between ~600 m.a.s.l and 2600 m.a.s.l., and extends over ~ 11% of the percolation facies extent and ~4% of the GrIS extent. High $T_{V,max}^B$, $T_{V,min}^B$,

https://doi.org/10.5194/tc-2021-116
Preprint. Discussion started: 30 April 2021

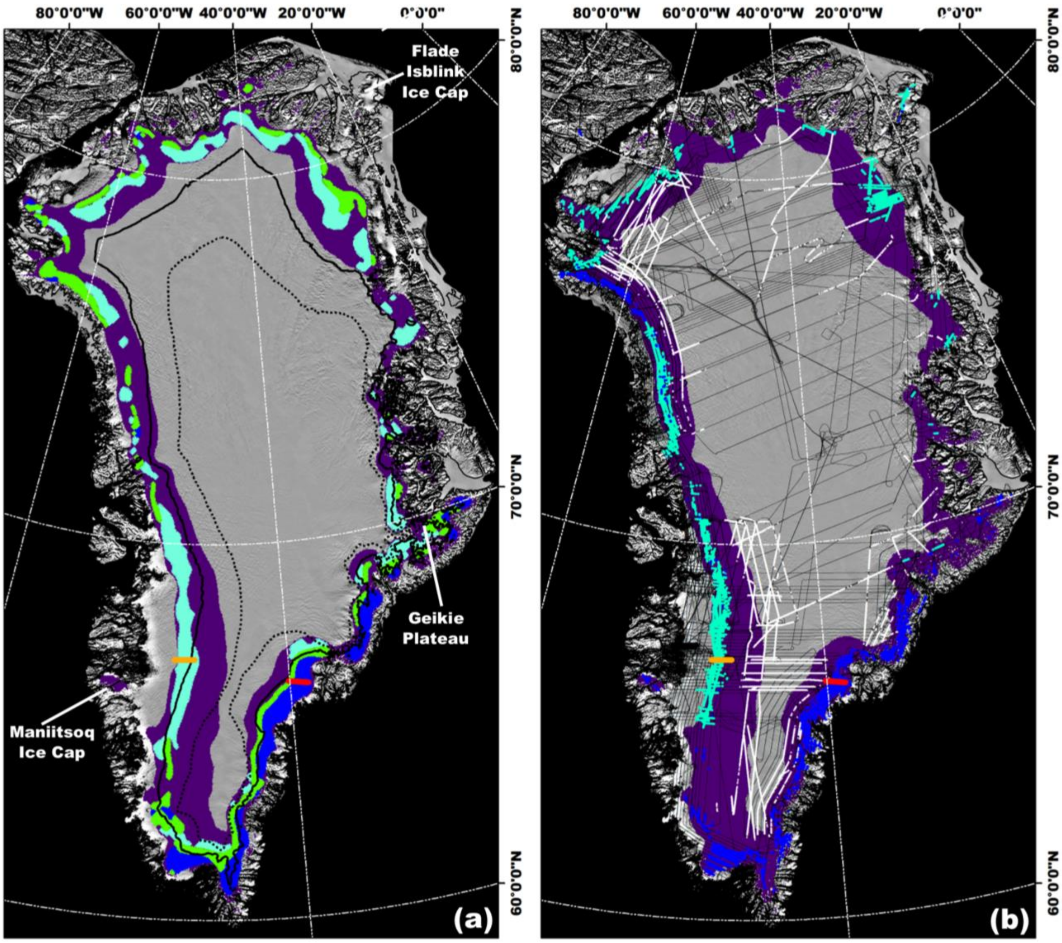

Figure 7

(a) The SMAP-derived perennial firn aquifer (blue shading), ice slab (cyan shading), perched firn aquifer (green shading), and percolation facies (purple shading) extents (2015-2019) generated by the adapted empirical algorithm overlaid on the 2015 MODIS Mosaic of Greenland image map (Haran et al., 2018). The black line is the 2000 m.a.s.l. contour, and the black dotted line is the 2500 m.a.s.l. contour (Howat et al., 2014). (b) The SMAP-derived extents are overlaid with AR- and MCoRDS-derived 2010-2017 perennial firn aquifer (blue shading; Miège et al., 2016), 2010-2014 ice slab (cyan shading; McFerrin et al., 2019), and 2012 spatially coherent melt layer (white shading; Culberg et al., 2021) detections along OIB flight lines (black lines). Overlapping perennial firn aquifer and ice slab detections are interpreted as perched firn aquifer areas. The red line is AR radargram profile along perennial firn aquifer transect A-B (Fig. 3a). The orange line is AR radargram profile along ice slab transect C-D (Fig. 3b).

https://doi.org/10.5194/tc-2021-116
Preprint. Discussion started: 30 April 2021

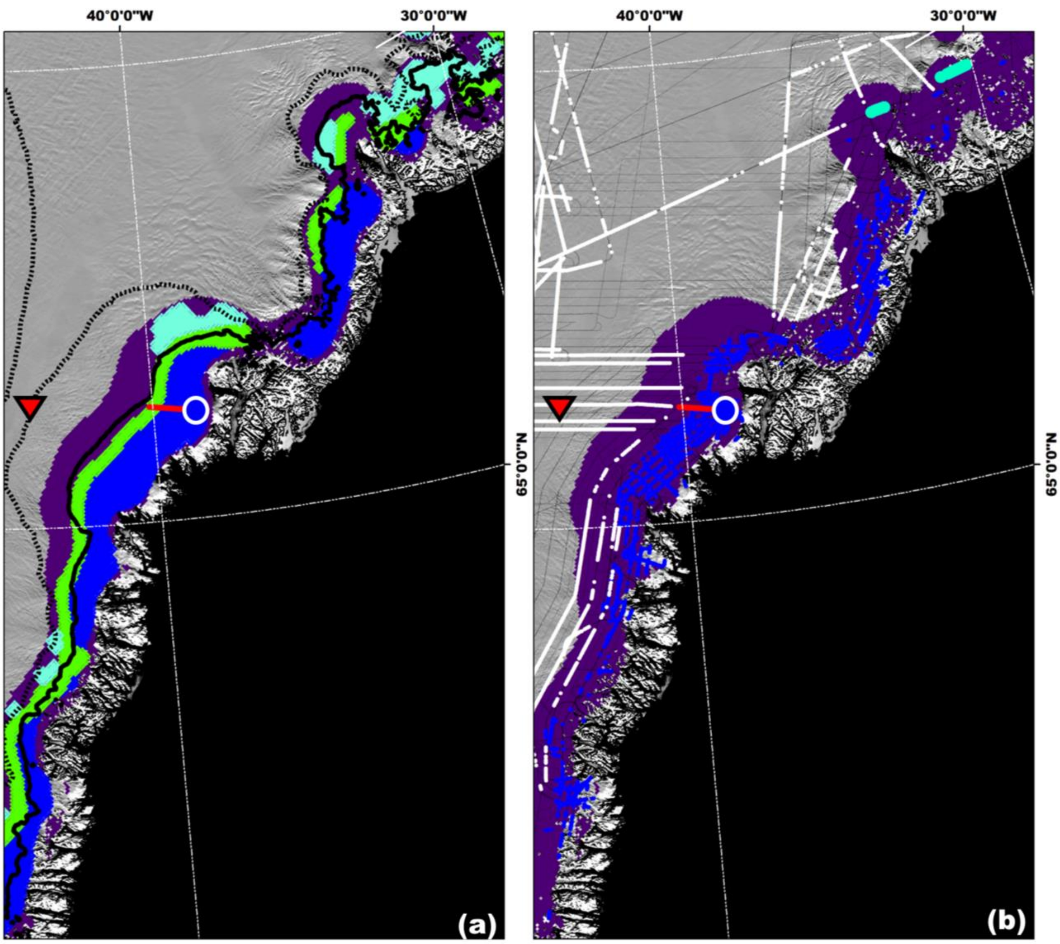

Figure 8

(a) The SMAP-derived perennial firn aquifer (blue shading), ice slab (cyan shading), perched firn aquifer (green shading), and percolation facies (purple shading) extents (2015-2019) generated by the adapted empirical algorithm over south eastern Greenland (Fig. 1c; zoom area in red box) overlaid on the 2015 MODIS Mosaic of Greenland image map (Haran et al., 2018). The solid black line is the 2000 m.a.s.l. contour, and the black dotted line is the 2500 m.a.s.l. contour (Howat et al., 2014). (b) The SMAP-derived percolation facies extent is overlaid with AR- and MCoRDS-derived 2010-2017 perennial firn aquifer (blue shading; Miège et al., 2016), 2010-2014 ice slab (cyan shading; McFerrin et al., 2019), and 2012 spatially coherent melt layer (white shading; Culberg et al., 2021) detections along OIB flight lines (black lines). Overlapping perennial firn aquifer and ice slab detections are interpreted as perched firn aquifer areas. The red line is AR radargram profile along perennial firn aquifer transect A-B (Figs. 1; 3a). The blue circle is a perennial firn aquifer area (Figs. 3a; 4a). The red triangle is a high-elevation (~2500 m.a.s.l.) percolation facies area (Figs. 4d).

https://doi.org/10.5194/tc-2021-116
Preprint. Discussion started: 30 April 2021

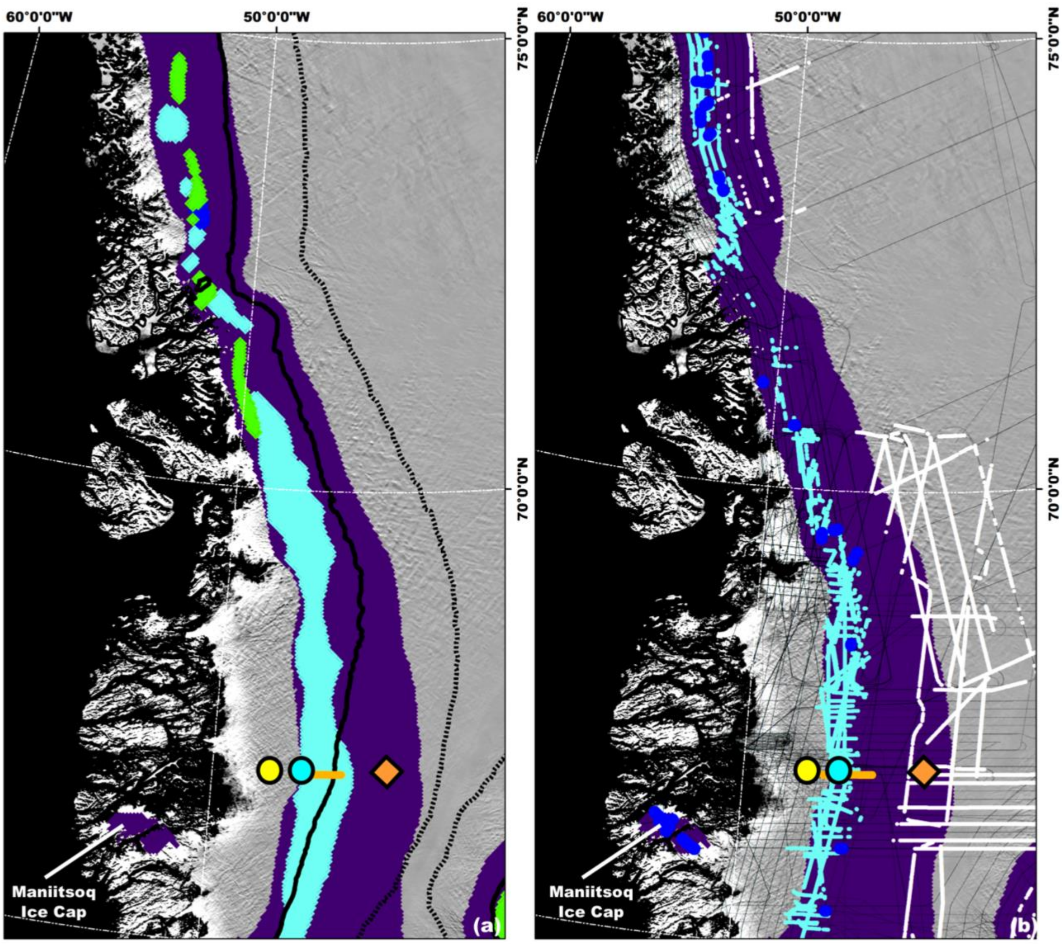

Figure 9

(a) The SMAP-derived perennial firn aquifer (blue shading), ice slab (cyan shading), perched firn aquifer (green shading), and percolation facies (purple shading) extents (2015-2019) generated by the adapted empirical algorithm over south western Greenland (Fig. 1c; zoom area in red box) overlaid on the 2015 MODIS Mosaic of Greenland image map (Haran et al., 2018). The solid black line is the 2000 m.a.s.l. contour, and the black dotted line is the 2500 m.a.s.l. contour (Howat et al., 2014). (b) The SMAP-derived percolation facies extent is overlaid with AR- and MCoRDS-derived 2010-2017 perennial firn aquifer (blue shading; Miège et al., 2016), 2010-2014 ice slab (cyan shading; McFerrin et al., 2019), and 2012 spatially coherent melt layer (white shading; Culberg et al., 2021) detections along OIB flight lines (black lines). Overlapping perennial firn aquifer and ice slab detections are interpreted as perched firn aquifer areas. The orange line is AR radargram profile along ice slab transect C-D (Figs 1; 3b). The cyan circle is a perched firn aquifer area (Figs. 3b; 4b). The orange diamond is a percolation facies area (Fig. 4c). The yellow circle is a superimposed ice area (Fig. 4e).

https://doi.org/10.5194/tc-2021-116
Preprint. Discussion started: 30 April 2021

The Cryosphere Discussions

ξ, and ζ values within the perennial firn aquifer extent indicates the presence of thicker water-saturated firn layers with larger volumetric fractions of meltwater that are radiometrically warm during both the melting and freezing seasons and have extended refreezing rates. The ice slab extent (76,000 km^2) is mapped at elevations between ~800 m.a.s.l and 2700 m.a.s.l., and extends over ~13 % of the percolation facies extent and ~4 % of the GrIS extent. As compared to perennial firn aquifer areas, decreased $T^B_{V,max}$, $T^B_{V,min}$, ξ and ζ values indicates the presence of thinner water-saturated firn layers with lower volumetric fractions of meltwater that are radiometrically colder and have slightly more rapid refreezing rates. The SMAP-derived perched firn aquifer calibration parameter intervals are within the perennial firn aquifer and the ice slab calibration parameter intervals (see Fig. 6, Table 3). The extents of these three sub-facies within the broader percolation facies are overlapping, such that perched firn aquifers typically represent the upper boundary of perennial firn aquifer areas that subsequently transition to percolation facies as well as the lower boundary of ice slab areas that subsequently transition to wet snow facies. However, in several areas in south and southeastern Greenland, the full progression of facies and sub-facies (dry snow facies - percolation facies - ice slab - perched firn aquifer - perennial firn aquifer – ablation facies) occur (e.g., Fig. 7a). The perched firn aquifer extent (37,000 km^2) is mapped at elevations between ~600 m.a.s.l and 2700 m.a.s.l., and extends over ~30% of perennial firn aquifer extent, ~24% of ice slab extent, ~2% of the percolation facies extent, and less than ~1% of the GrIS extent. Combined together, the total extent (~140,000 km^2) is the equivalent of ~24% of the percolation facies extent and 10% of the GrIS extent. This increases previous AR- and MCoRDS-derived elevation estimates upslope ~600 m.a.s.l. in both perennial firn aquifer areas (Miège et al., 2016) and ice slab areas (McFerrin et al., 2019). The highest perennial firn aquifer, ice slab, and perched firn aquifer elevations (>2500 m.a.s.l.) are mapped in southern Greenland and on the Geikie plateau, in central eastern Greenland.

Table 4. *The SMAP-derived perennial firn aquifer, ice slab, and perched firn aquifer extents (2015-2019) over the percolation facies and the GrIS, and the elevation range at which they are mapped.*

	Percolation Facies Extent (%)	Ice Sheet Extent (%)	Elevation Range (m.a.s.l.)
Perennial Firn Aquifers	11	4	600 – 2600
Ice Slabs	13	4	800 – 2700
Perched Firn Aquifers	5	<1	600 – 2700

Figs. 7b-9b shows perennial firn aquifers (blue shading), ice slabs (cyan shading), and spatially coherent melt layers (white shading) detected by airborne ice-penetrating radar surveys (2010-2017) overlaid on the SMAP-derived percolation facies extent (2015-2019)**.** Perched firn aquifer areas are inferred where perennial firn aquifer and ice slab detections overlap. The SMAP-derived perennial firn aquifer extent mapped in southern, and south and central eastern Greenland is consistent with the AR- and MCoRDS-geophysical derived perennial firn aquifer detections (2010-2017), except in north western Greenland where perched firn aquifers are alternatively mapped. The SMAP-derived ice slab extent mapped in western, central and north eastern, and northern Greenland is generally consistent with the spatial patterns of the AR-derived ice slab detections (2010-2014), however, is significantly expanded upslope in each of these areas. We note that the AR-derived ice slab detections are limited in space and time, particularly in northern Greenland, with a time interval as large as nine years between the airborne ice penetrating radar surveys and the SMAP enhanced-resolution T_V^B imagery used in the adapted empirical algorithm (i.e., 2010 to 2019). In western and northern Greenland, the 2015 melting season was especially intense (Tedesco et al., 2016). And, in northern Greenland, the ablation facies have recently increased in extent (2010-2019; Noël et al., 2019), and supraglacial lakes have recently advanced inland (2014-2019; Turton et al., 2021), indicating a likley geophysical basis for the observed upslope expansion. In central and north eastern, and northern Greenland, perched firn aquifers are often alternatively mapped. Additional smaller ice slab areas are mapped in south and south eastern (Figs. 9a; 9b) Greenland. The scattered SMAP-derived perched firn aquifer extent mapped in north western and central eastern Greenland is fairly consistent with the sparse AR- and MCoRDS-derived perched firn aquifer detections (2010-2017), however, in central western Greenland (Figs. 9a; 9b) ice slab areas are alternatively mapped. Expansive additional perched firn aquifer areas are mapped in southern, and south and central eastern Greenland. These areas are often coincident with spatially coherent melt layer detections, particularly in south eastern Greenland (Figs. 8a, 8b). Neither perennial firn aquifer, ice slab, nor perched firn aquifer areas are mapped on the Maniitsoq and Flade Isblink Ice Caps. Over these two small ice caps, L-band emissions spatially integrated with emissions from rock, land, the ocean, and adjacent percolation facies and wet snow facies areas result in SMAP-derived calibration parameter values outside the defined intervals for each of these sub-facies.

We infer that the SMAP-derived perched firn aquifer extent represents L-band emissions from: (1) spatially expansive, relatively shallow water-saturated firn layers with lower volumetric fractions of meltwater as compared to perennial firn aquifer areas. These shallow water-saturated firn layers transiently form on top of buried ice slabs, spatially coherent melt layers, or other semi-impermeable layers that have previously formed within the upper snow and firn layers of the percolation facies, as shown in Figs. 7-8. Or, (2) spatially scattered deeper water-saturated firn layers with larger volumetric fractions of meltwater (i.e., perennial firn aquifers) that are spatially integrated with L-band emissions from adjacent ice slabs, percolation facies, and/or wet snow facies areas. These areas are observed as shallow water-saturated firn layers with lower volumetric fractions of meltwater over SMAP's ~18 km footprint (i.e., the effective resolution). Or, (3) a combination of these englacial firn hydrological features, which is a likely scenario over many perched firn aquifers areas. This is particularly likely in north western Greenland, where airborne ice penetrating radar surveys consistently detect perennial firn aquifers; however, the SMAP-derived extent indicates perched firn aquifer areas (Fig. 7).

https://doi.org/10.5194/tc-2021-116
Preprint. Discussion started: 30 April 2021

The Cryosphere Discussions

Shallow buried supraglacial lakes have recently been identified within the percolation facies of western, northern, and north and central eastern Greenland using airborne ice penetrating radar surveys (Koenig et al., 2015) and satellite synthetic aperture radar imagery (Miles et al., 2017; Schröder et al., 2020; Dunmire et al., 2021). These buried supraglacial lakes are within the SMAP-derived perennial firn aquifer, ice slab, and perched firn aquifer extents, however, they are not expected to significantly influence L-band emissions in these areas for two reasons: (1) as compared to SMAP's ~18 km footprint, the mean extent of buried supraglacial lakes is limited (less than ~1 km^2), and they are sparsely distributed in perennial firn aquifer, ice slab, and perched firn aquifer areas (Dunmire et al., 2021). (2) Supraglacial lakes form during the melting season as a result of meltwater storage in topographic depressions at the ice sheet surface (Echelmeyer et al. 1991). Similar to subglacial lakes (Jezek et al., 2015) and perennial firn aquifers (Miller et al., 2020), supraglacial lakes represent radiometrically cold subsurface meltwater reservoirs. Upwelling L-band emissions from deeper firn layers, glacial ice, and the underlying bedrock are effectively blocked by high reflectivity and attenuation at the impermeable layer-lake bottom interface. This results in a low observed T_V^B at the upper surface of meltwater stored within supraglacial lakes. During the freezing season, the upper surface of meltwater stored within supraglacial lakes refreezes and forms a partial or solid-ice cap that is sometimes buried by snow accumulation (Koenig et al., 2015). Airborne ice penetrating radar surveys in April and May between 2009 and 2012 suggest the mean depth to the upper surface of meltwater stored within buried supraglacial lakes is ~2 m (Koenig et al., 2015). As previously noted, over perennial firn aquifer, ice slab, and perched firn aquifer areas, L-band emissions from the radiometrically warm upper snow and firn layers decrease on variable time scales during the freezing season as embedded ice structures slowly refreeze at increased depths below the ice sheet surface and induce strong volume scattering (Rignot et al., 1993; Rignot 1995). T_V^B can decrease by as much as ~50 K during the freezing season (e.g., Fig. 4a), representing the descent of the upper surface of stored meltwater by ~tens of meters (Miège et al., 2016). However, over buried supraglacial lakes, L-band emissions from the refreezing partial or solid-ice cap, which is smooth relative to the L-band wavelength (~21 cm), induce surface scattering. As a result, T_V^B decreases over buried supraglacial lakes are negligible. Thus, over SMAP's ~18 km footprint, water-saturated firn layers dominate L-band emissions over the percolation facies of the GrIS.

The SMAP-derived perennial firn aquifer extent (~64,000 km^2) generated by our adapted empirical algorithm and the multi-year (2010-2017) calibration technique is consistent with the extent (~66,000 km^2) generated by the previously developed empirical algorithm and the single-coincident year (2016) calibration technique described in Miller et al., 2020. The SMAP-derived perennial firn aquifer extent is generally consistent with previous C-band (5.3 GHz) satellite radar scatterometer-derived perennial firn aquifer extents mapped using the Advanced SCATterometer (ASCAT) on the European Organization for the Exploitation of Meteorological Satellites (EUMETSAT) Meteorological Operational A (MetOp-A) satellite (2009-2016, ~52 000-153 000 km^2; Miller, 2019), and the Active Microwave Instrument in radar scatterometer mode (ESCAT) on ESA's European Remote Sensing (ERS) satellite series (1992-2001, ~37 000-64 000 km^2; Miller, 2019) as well as the C-band (5.4 GHz) synthetic aperture radar-derived extent

https://doi.org/10.5194/tc-2021-116
Preprint. Discussion started: 30 April 2021

mapped using ESA's Sentinel-1 satellite (2014-2019, ~54 000 km^2; Brangers et al., 2020). The exception is the ASCAT-derived perennial firn aquifer extent (2012-2013, ~153,000 km^2; Miller et al., 2019) mapped following the anomalous 2012 melting season (Nghiem et al., 2012) in which significant changes in the dielectric and geophysical properties that influence radar backscatter and the temporal C-band signatures occurred. The unreasonably expansive (i.e., more than twice the mean) mapped extent is a result of ASCAT'S shallow (~several meters) C-band penetration depth (Jezek et al., 1994), and the simple threshold-based algorithm that was not calibrated for an extreme melting season that included saturation of the upper snow and firn layers of the dry snow facies and percolation facies with relatively large volumetric fractions of meltwater (Miller et al., 2019). Water-saturated firn layers had extended refreezing rates, however, seasonal meltwater was not stored at depth. Spatially coherent melt layers were alternatively formed in many of the mapped areas (Culberg et al., 2021). The SMAP-derived ice slab extent (~76,000 km^2) is also consistent with previous AR-derived ice slab extents (2010-2014, ~64,800 km^2-69,400 km^2; McFerrin et al., 2019).

Although we simply consider our mapped extents a high-probability area for preferential formation, the maps generated by our adapted empirical algorithm and the multi-year (2010-2017) calibration technique for individual years suggest interannual variability in perennial firn aquifer, ice slab, and perched firn aquifer extents, which is summarized in Table 5. Our results demonstrate reasonable sensitivity to variability in the dielectric and geophysical properties that influence the radiometric temperature and temporal L-band signatures, even during the extreme 2015 melting season (Tedesco et al., 2016).

Table 5 *The SMAP-derived perennial firn aquifer, ice slab, and perched firn aquifer extents (2015-2019).*

	Perennial Firn Aquifer Extent (km^2)	Ice Slab Extent (km^2)	Perched Firn Aquifer Extent (km^2)
2015-2019	66,000	76,000	37,000
2015-2016	63,000	23,000	17,000
2016-2017	69,000	48,000	38,000
2017-2018	73,000	27,000	20,000
2018-2019	70,000	38,000	26,000

5 Summary and Future Work

L-band satellite microwave sensors – including NASA's L-band SMAP mission - represent a relatively new Earth-observation tool that has exceptional capabilities for cryospheric applications. Especially, mapping englacial and subglacial hydrological features at depths of ~tens to hundreds of meters beneath the surface of Earth's polar ice sheets. In this study, for the first time, we have exploited this capability and demonstrated the novel use of the L-band microwave radiometer on NASA's SMAP satellite for mapping perennial firn aquifers, ice slabs, and perched firn aquifers together as a continuous system over the percolation facies of the GrIS. We have also demonstrated that SMAP enhanced-resolution L-band T_V^B imagery can effectively resolve percolation facies features that are not effectively resolved in conventionally processed SMAP L-band T_V^B imagery (e.g., Fig. 1). We have adapted our previously developed empirical algorithm (Miller et al., 2020) by expanding our analysis of spatiotemporal differences in SMAP enhanced-resolution T_V^B imagery and temporal L-band signatures over the GrIS. We have used this analysis to derive a firn saturation parameter from a simple two-layer L-band geophysical-brightness temperature model. And, we have used the firn saturation parameter to map the extent of the percolation facies. We have found that by correlating maximum and minimum T_V^B values, the firn saturation parameter, and the refreezing rate parameter with perennial firn aquifer, ice slab, and perched firn aquifer detections identified via NASA's OIB campaigns that we can calibrate our previously developed empirical algorithm (Miller et al., 2020) to map plausible extents.

We note that significant uncertainty exists in the mapped extents as a result of (1) correlating the SMAP-derived parameters with airborne ice-penetrating radar detections that are not coincident in time, (2) the lack of a distinct temporal L-band signature delineating the boundary between each of the mapped sub-facies within the broader percolation facies, and (3) the much more limited extent of the airborne ice-penetrating radar detections as compared to the rSIR grid cell extent, as well as the effective resolution of the SMAP enhanced-resolution T_V^B imagery. Additional uncertainty exists in the perched firn aquifer extent as a result of fitting L-band signatures to the continuous logistic model, which is not optimal for these specific sub-facies.

Miller et al., (2020) normalized SMAP enhanced-resolution T_V^B time series and converted the exponential rate of T_V^B decrease over perennial firn aquifer areas to a binary parameter to map extent. In this study, we have converted the SMAP-derived parameters to binary parameters to map the extent of perennial firn aquifer, ice slab, and perched firn aquifer areas. Moreover, we have included additional analysis of the spatiotemporal differences in maximum and minimum T_V^B values, the firn saturation parameter, and the refreezing rate parameter. We have shown that spatiotemporal differences in the SMAP-derived parameters are consistent with our assumption of spatiotemporal differences in the englacial hydrology and thermal characteristics of firn layers at depth. Particularly, our assumption that latent heat release influences temporal L-band signatures within the percolation facies of the GrIS. This includes continuous latent heat release via the slow refreezing of the deeper firn layers in perennial and perched firn aquifer areas that are saturated with large volumetric fractions of meltwater. And, latent heat release that

https://doi.org/10.5194/tc-2021-116
Preprint. Discussion started: 30 April 2021

occurs throughout the percolation facies via more rapid refreezing of seasonal meltwater by the descending winter cold wave, and the subsequent formation of embedded ice structures, including ice slabs and spatially coherent melt layers, within the upper snow and firn layers.

Future work will focus on simulating maximum and minimum T_V^B, the firn saturation parameter, and the refreezing rate parameter as well as temporal L-band signatures observed over perennial firn aquifer, ice slab, and perched firn aquifer areas within the percolation facies of the GrIS for a wide range of geophysical properties. Significant interannual variability in the dielectric and geophysical properties that seasonally influence the radiometric temperature and temporal L-band signatures can occur, particularly following extreme melting seasons, such that it is critical that these properties are understood and considered in any given year. To better interannual variability as well as other geophysical properties, we will interpret our results together with climatological parameters, such as snow accumulation, liquid water content, temperature, and surface mass balance, and over the GrIS simulated using the Regional Atmospheric Climate Model (RACMO2.3p2; Noël et al., 2018). Additionally, we will simulate the distinct temporal L-band signatures observed over spatially coherent melt layers in the upper snow and firn layers of the dry snow facies and percolation facies of the GrIS recently identified via MCoRDS flown by NASA's OIB campaigns (Culberg et al., 2021) following the anomalous 2012 melting season (Nghiem et al., 2012) and as well as explore the potential for mapping the extent of these near-surface englacial hydrological features using satellite L-band microwave radiometry. Nghiem et al., (2003) previously demonstrated mapping spatially coherent melt layers that were formed following the anomalous 2002 melting season (Steffen et al., 2004) using similar signatures observed in Ku-band radar backscatter time series collected by the SeaWinds radar scatterometer that was flown on NASA's QuikSCAT satellite (Tsai et al., 2000). Combining multi-layer depth-integrated L-band geophysical-brightness temperature models (e.g., Jezek et al., 2015) that include embedded ice structure parametrizations (e.g., Jezek et al., 2018) with models of depth-dependent geophysical parameters can lead to an improved understanding of the extremely complex and very poorly described physics controlling L-band emissions over the percolation facies of the GrIS. For L-band emissions over perennial firn aquifer, ice slab, perched firn aquifer, and spatially coherent melt layer areas, the key geophysical parameters include atmospheric temperature forcing, physical temperature versus depth, latent heat, snow accumulation, the volumetric fraction and depth of meltwater, and the volumetric fraction and geometric configuration of embedded ice structures. The development of more sophisticated empirical algorithms that incorporate multi-layer depth-integrated L-band geophysical-brightness temperature models that are constrained by in situ measurements can help reduce the significant uncertainty in the current mapped extents, and provide more accurate boundaries delineating each of these sub-facies within the broader percolation facies that can be used to quantify variability in extent. As Greenland's climate continues to warm, and seasonal surface melting increases in extent, intensity, and duration, quantifying the possible rapid expansion of each of these sub-facies using satellite L-band microwave radiometry has significant implications for understanding ice sheet-wide variability in englacial firn hydrology resulting in meltwater-induced hydrofracturing and accelerated ice flow as well as high-elevation run-off that can impact the mass balance and stability of the GrIS.

The results presented in this study demonstrate the outstanding potential of L-band satellite microwave sensors for mapping englacial firn hydrological features within the percolation facies of the GrIS that can be extended to forthcoming satellite missions, such as the NASA-ISRO SAR mission (NISAR), ESA's Copernicus Imaging Microwave Radiometer (CIMR) mission, ESA's Copernicus Radar Observation System for Europe in L-band (ROSE-L) mission, and candidate missions, such as ESA's Earth Explorer 10 Cryorad mission.

Data Availability

SMAP enhanced-resolution L-band T_V^B imagery (2015-2019) have been produced as part of the NASA Science Utilization of SMAP project and are available at https://doi.org/10.5067/QZ3WJNOUZLFK (Brodzik et al., 2019). The NASA MEaSUREs Greenland Ice Mapping Project (GIMP) Land Ice and Ocean Classification Mask, Version 1, is available at https://doi.org/10.5067/B8X58MQBFUPA (Howat, 2017), and the Digital Elevation Model, Version 1, is available at https://nsidc.org/data/nsidc-0645/versions/1 (Howat et al., 2015). The coastline data are available from GSHHG – A Global Self-consistent, Hierarchical, High-resolution Geography Database https://doi.org/10.1029/96JB00104 (Wessel and Smith, 1996). Ice surface temperature imagery (2015-2019) have been produced as part of the Multilayer Greenland Ice Surface Temperature, Surface Albedo, and Water Vapor from MODIS V001 data set and are available at https://doi.org/10.5067/7THUWT9NMPDK (Hall and DiGirolamo, 2019). OIB AR- and MCoRDS-derived perennial firn aquifers detections (2010-2017) are available at https://arcticdata.io/catalog/view/doi:10.18739/A2985M (Miège et al., 2016). OIB AR-derived ice slab detections (2010-2014) are available at https://doi.org/10.6084/m9.figshare.8309777 (McFerrin et al., 2019). OIB AR-derived spatially coherent melt layer detections (2017) are available at (https://doi.org/10.18739/A2736M33W) (Culberg et al., 2021). OIB AR L1B Geolocated Radar Echo Strength Profiles, Version 2, are available at, https://doi.org/10.5067/0ZY1XYHNIQNY (Paden et al., 2018). NASA MEaSUREs MODIS Mosaic of Greenland (MOG) 2015 Image Map, Version 2, is available at https://nsidc.org/data/NSIDC-0547/versions/2 (Haran et al., 2018). SMAP-derived perennial firn aquifer, ice slab, and perched firn aquifer extents are available from JZM upon request.

Author Contributions

JZM initiated the study, adapted the empirical model, performed the analyses, and wrote the manuscript. RC processed and interpreted the OIB AR radargram profiles. RC and DMS provided the spatially coherent melt layer detections. All authors participated in discussions and reviewed manuscript drafts.

https://doi.org/10.5194/tc-2021-116
Preprint. Discussion started: 30 April 2021

Competing Interests

The authors declare that they have no conflict of interest.'

Financial Support

JZM, DGL, and MJB are supported by the NASA SMAP science team (no. 80NSSC20K1806), and by the NASA Cryospheric Science Program (no. 80NSSC18K1055 and no. 80NSSC21K0749) under grants to the University of Colorado and Brigham Young University. RC is supported by a National Defense Science and Engineering Graduate Fellowship. RC and DMS are supported in part by NASA (no. NNX16AJ95G and NSF (no. 1745137). CAS is supported by the NASA Headquarters Cryospheric Science Program. We acknowledge the use of data from CReSIS generated with support from the University of Kansas, NASA Operation IceBridge grant NNX16AH54G, NSF grants ACI-1443054, OPP-1739003, and IIS-1838230, Lilly Endowment Incorporated, and Indiana METACyt Initiative.

References

Abdalati, W., and Steffen, K.: Snowmelt on the Greenland Ice Sheet as derived from passive microwave satellite data, J. Climate, 10, 165-175, https://doi.org/10.1175/1520-0442(1997)010<0165:SOTGIS>2.0.CO;2, 1997.

Alley, R. B., Dupont, T. K., Parizek, B. R., Anandakrishnan, S.: Access of surface meltwater to beds of sub-freezing glaciers: Preliminary insights, Ann. Glaciol., 40, 8-14, https://doi.org/10.3189/172756405781813483, 2005.

Ashcraft, I. and Long, D.: Comparison of methods for melt detection over Greenland using active and passive microwave measurements, Int. J. Remote Sens., 27, 2469-2488, https://doi.org/10.1080/01431160500534465, 2006.

Benson, C. S.: Stratigraphic studies in the snow and firn of the Greenland Ice Sheet, Ph.D. thesis, California Institute of Technology, 228 pp., 1960.

Bindschadler, R. A., Jezek, K. C., and Crawford, J.: Glaciological investigations using the synthetic aperture radar imaging system, Ann. Glaciol., 9, 11-19. https://doi.org/10.1017/S0260305500200694, 1987.

Brangers, I., Lievens, H., Miège, C., Demuzere, M., Brucker, L., and De Lannoy, G. J. M.: Sentinel-1 detects firn aquifers in the Greenland Ice Sheet, Geophys. Res. Lett., 47, e2019GL085192, https://doi.org/10.1029/2019GL085192, 2020.

Brodzik, M. J., Long, D. G., and Hardman, M. A.: SMAP Radiometer Twice-Daily rSIR-Enhanced EASE-Grid 2.0 Brightness Temperatures, Version 1, NASA National Snow and Ice Data Center Distributed Active Archive Center,https://doi.org/10.5067/QZ3WJNOUZLFK, 2019.

Brodzik, M. J., Billingsley, B., Haran, T., Raup, B., and Savoie, M. H.: EASE-Grid 2.0: Incremental but significant improvements for Earth-gridded data sets, ISPRS Int. J. Geo-Inf., 1, 32-45, https://doi.org/10.3390/ijgi1010032, 2012.

https://doi.org/10.5194/tc-2021-116
Preprint. Discussion started: 30 April 2021

Chu, W., Schroeder, D. M., and Siegfried, M. R.: Retrieval of englacial firn aquifer thickness from ice-penetrating radar sounding in southeastern Greenland, Geophys. Res. Lett., 45, 11,770-11,778, https://doi.org/10.1029/2018GL079751, 2018.

CReSIS: CReSIS radar depth sounder data, Digital Media, http://data.cresis.ku.edu/, 2016.

Colgan, W., Rajaram, H., Abdalati, W., McCutchan, C., Mottram, R., Moussavi, M. S., and Grigsby, S.: Observations, models, and mass balance implications: Glacier crevasses, Rev. Geophys., 54, 119-161, https://doi.org/10.1002/2015RG000504, 2016.

Culberg, R., Schroeder, D.M. and Chu, W.: Extreme melt season ice layers reduce firn permeability across Greenland, Nat Commun, **12,** 2336, https://doi.org/10.1038/s41467-021-22656-5, 2021

Culberg, R.: Refrozen melt layer location, density, and connectivity records from airborne radar sounding, Greenland, NSF Arctic Data Center, https://doi.org/10.18739/A2736M33W, 2021.

Cullather, R. I., Andrews, L. C., Croteau, M. J., Digirolamo, N. E., Hall, D. K., Lim, Y., Loomis, B. D., Shuman, C. A., and Nowicki, S. M. J.: Anomalous circulation in July 2019 resulting in mass loss on the Greenland Ice Sheet. Geophys. Res. Lett., 47, https://doi.org/10.1029/2020GL087263, 2020.

Das, S. B., Joughin, I., Behn, M. D., Howat, I. M., King, M. A., Lizarralde, D., Bhatia, M. P., Fracture propagation to the base of the Greenland Ice Sheet during supraglacial lake drainage, Science, 320, 778-781, https://doi.org/10.1126/science.1153360, 2008.

Drinkwater, M. R., Long, D. G., and Bingham, A. W.: Greenland snow accumulation estimates from satellite radar scatterometer data, J. Geophys. Res. Atmos., 106, 33935-33950. https://doi.org/10.1029/2001JD900107, 2001.

Dunmire, D., Banwell, A. F., Lenaerts, J. T. M., and Datta, R. T.: Contrasting regional variability of buried meltwater extent over two years across the Greenland Ice Sheet, The Cryosphere Discuss, https://doi.org/10.5194/tc-2021-3, in review, 2021.

Early, D. S., and Long, D. G.: Image reconstruction and enhanced-resolution imaging from irregular samples, IEEE Trans. Geosci. Remote Sens. 39, 291-302, https://doi.org/10.1109/36.905237, 2001.

Echelmeyer, K., Clarke, T. S., and Harrison, W. D.: Surficial glaciology of Jakobshavn Isbræ, West Greenland 1. Surface morphology, J. Glaciol., 37, 368–382, https://doi.org/10.1017/S0022143000005803, 1991.

Entekhabi, D., et al.: The Soil Moisture Active Passive (SMAP) Mission, Proc. IEEE, 98, 704-716, https://doi.org/10.1109/JPROC.2010.2043918, 2010.

Fahnestock, M., Bindschadler, R., Kwok, R., and Jezek, K.: Greenland Ice Sheet surface properties and ice dynamics from ERS-1 SAR imagery. Science, 262, 1530-1534. https://doi.org/10.1126/science.262.5139.1530, 1993.

Forster, R. R., Box, J. E., Van Den Broeke, M. R., Miège, C., Burgess, E. W., Van Angelen, J. H., Lenaerts, J. T. M., Koenig, L. S., Paden, J., Lewis, C., Gogineni, S. P., Leuschen, C., and McConnell, J. R.: Extensive liquid meltwater storage in firn within the Greenland Ice Sheet, Nat. Geosci., 7, 95–98, https://doi.org/10.1038/ngeo2043, 2014.

Fountain, A. G., and Walder, J. S.: Water flow through temperate glaciers. Rev. of Geophys., 36, 299-328, https://doi.org/10.1029/97RG03579, 1998.

Freilich, M. H., Long, D. G., and Spencer, M. W.: SeaWinds: A scanning scatterometer for ADEOS-II science overview, Proc. IEEE, 1994, 960-963, https://doi.org/10.1109/IGARSS.1994.399313, 1994.

https://doi.org/10.5194/tc-2021-116
Preprint. Discussion started: 30 April 2021

Franco, B., Fettweis, X., and Erpicum, M.: Future projections of the Greenland ice sheet energy balance driving the surface melt, The Cryosphere, 7, 1–18, https://doi.org/10.5194/tc-7-1-2013, 2013

Goward, S. N., Masek, J. G., Williams, D. L., Irons, J. R., and Thompson, R. J.: The Landsat 7 mission: Terrestrial research and applications for the 21st century. Remote Sensing of Environment, 78, 3-12. https://doi.org/10.1016/S0034-4257(01)00262-0, 2001.
Hall, D. K., and DiGirolamo, N.: Multilayer Greenland Ice Surface Temperature, Surface Albedo, and Water Vapor from MODIS, Version 1, NASA National Snow and Ice Data Center Distributed Active Archive Center, https://doi.org/10.5067/7THUWT9NMPDK, 2019.

Hall, D. K., Comiso, J. C., Digirolamo, N. E., Shuman, C. A., Key, J. R., and Koenig, L. S.: A satellite-derived climate-quality data record of the clear-sky surface temperature of the Greenland Ice Sheet, J. Clim., 25, 4785–4798, https://doi.org/10.1175/JCLI-D-11-00365.1, 2012.

Hanna, E., Navarro, F. J., Whitehouse, P. L., Zwally, H. J., Pattyn, F., Domingues, C. M., Fettweis, X., Ivins, E. R., Nicholls, R. J., Ritz, C., Smith, B., and Tulaczyk, S.L: Ice-sheet mass balance and climate change, Nature, 498, 51-59, https://doi.org/10.1038/nature12238, 2013.

Haran, T., Bohlander J., Scambos T., Painter, T., and Fahnestock, M.: MEaSUREs MODIS Boulder, Colorado USA. NASA National Snow and Ice Data Center Distributed Active Archive Center, https://doi.org/10.5067/9ZO79PHOTYE5, 2018.

Harper, J., Humphrey, N., Pfeffer, W. T., Brown, J., and Fettweis, X.: Greenland ice-sheet contribution to sea-level rise buffered by meltwater storage in firn, Nature, 491, 240–243, https://doi.org/10.1038/nature11566, 2012.

Hicks, B. R., and Long, D. G.: Inferring Greenland melt and refreeze severity from SeaWinds scatterometer data, Int. J. Remote Sensing, 32, 8053-8080, https://doi.org/10.1080/01431161.2010.532174, 2011.

Howat, I.: MEaSUREs Greenland Ice Mapping Project (GIMP) Land Ice and Ocean Classification Mask, Version 1, NASA National Snow and Ice Data Center Distributed Active Archive Center, https://doi.org/10.5067/B8X58MQBFUPA, 2017.

Howat, I., Negrete, A., and Smith, B.: MEaSUREs Greenland Ice Mapping Project (GIMP) Digital Elevation Model, Version 1, NASA National Snow and Ice Data Center Distributed Active Archive Center, doi: https://doi.org/10.5067/NV34YUIXLP9W, 2015.

Howat, I., Negrete, A., and Smith, B.: The Greenland Ice Mapping Project (GIMP) land classification and surface elevation datasets, The Cryosphere, 8, 1509-1518, https://doi.org/10.5194/tc-8-1509-2014, 2014.

Humphrey, N. F., Harper, J. T., and Pfeffer, W. T.: Thermal tracking of meltwater retention in Greenland's accumulation area, J. Geophys. Res., 117, https://doi.org/10.1029/2011JF002083, 2012.

Jezek, K. C., Drinkwater M. R., Crawford, J. P., Bindshandler, R., and Kwok, R.: Analysis of synthetic aperture radar data collected over the southwestern Greenland Ice Sheet. J. of Glaciol, 39, 119-132, https://doi.org/10.1017/S002214300001577X, 1993.

Jezek, K. C., Gogineni, P., and Shanableh, M.: Radar measurements of melt zones on the Greenland Ice Sheet, Geophys. Res. Lett., 21, 33-36, https://doi.org/10.1029/93GL03377, 1994.

Jezek, K. C., Johnson, J. T., Drinkwater, M. R., Macelloni, G., Tsang, L., Aksoy, M., and Durand M.: Radiometric approach for estimating relative changes in intraglacier average temperature, IEEE Trans. Geosci. Remote Sens., 53, 134-143, https://doi.org/10.1109/TGRS.2014.2319265, 2015.

Jezek, K. C., Johnson J. T., Tan S., Tsang L., Andrews, M. J., Brogioni, M., Macelloni, G., Durand, M., Chen, C. C., Belgiovane, D. J., Duan, Y., Yardim, C., Li, H., Bringer, A., Leuski, V., and Aksoy, M.: 500–2000-MHz brightness temperature spectra of the northwestern Greenland Ice Sheet, IEEE Trans. Geosci. Remote Sens., 56, 1485-1496, https://doi.org/10.1109/TGRS.2017.2764381, 2018.

Jones, W. L., Schroeder, L. C., Boggs, D. H., Bracalente, E. M., Brown, R. A., Dome, G. J., Pierson, W. J., and Wentz, F. J.: The SEASAT-A satellite scatterometer: The geophysical evaluation of remotely sensed wind vectors over the ocean: J. Geophys. Res. Oceans, 87, 3297-3317, https://doi.org/10.1029/JC087iC05p03297, 1982.

Joughin, I., Das, S. B., Flowers, G .E., Behn, M. D., Alley, R. B., King, M. A., Smith, B. E., Bamber, J. L., van den Broeke, M. R., and Van Angelen, J. H.: Influence of ice-sheet geometry and supraglacial lakes on seasonal ice-flow variability, The Cryosphere, 7, 1185-1192, https://doi.org/10.5194/tc-7-1185-2013, 2013.

Joughin, I., Das, S. B., King, M. A., Smith, B. E., Howat, I. M., and Moon, T.: Seasonal speedup along the western flank of the Greenland Ice Sheet, Science, 320, 781-783, https://doi.org/10.1126/science.1153288, 2008.

Kerr, Y. H., Waldteufel, P., Wigneron, J., Martinuzzi, J., Font, J., and Berger, M.: Soil moisture retrieval from space: The Soil Moisture and Ocean Salinity (SMOS) mission, IEEE Trans. Geosci. Remote Sens., 39, 1729-1735, https://doi.org/10.1109/36.942551, 2001.

Koenig, L. S., Miège, C., Forster, R. R., and Brucker, L.: Initial in situ measurements of perennial meltwater storage in the Greenland firn aquifer, Geophys. Res. Lett., 41, 81-85, https://doi.org/10.1002/2013GL058083, 2014.

Kuipers Munneke, P. K., Ligtenberg, S. R. M., Van Den Broeke, M. R., Van Angelen, J. H., and Forster, R. R.: Explaining the presence of perennial liquid water bodies in the firn of the Greenland Ice Sheet, Geophys. Res. Lett., 41, 476–483, https://doi.org/10.1002/2013GL058389, 2014.

Le Vine, D. M., Lagerloef, G. S. E., and Torrusio, S. E.: Aquarius and remote sensing of sea surface salinity from space, Proc. IEEE, 98, 688-703, https://doi.org/10.1109/JPROC.2010.2040550, 2010.

Lewis, C., Gogineni, S., Rodriguez-Morales, F., Panzer, B., Stumpf, T., Paden, J., and Leuschen, C.: Airborne fine-resolution UHF radar: An approach to the study of englacial reflections, firn compaction and ice attenuation rates, J. Glaciology, 61, 89-100. https://doi.org/10.3189/2015JoG14J089, 2015.

Long, D. G., Brodzik, M. J., and Hardman M. A.: Enhanced-resolution SMAP brightness temperature image products, IEEE Trans. Geosci. Remote Sens., 57, 4151-4163, https://doi.org/10.1109/TGRS.2018.2889427, 2019.

Long, D. G., and Brodzik, M. J.: Optimum image formation for spaceborne microwave radiometer products, IEEE Trans. Geosci. Remote Sens., 54, 2763-2779. https://doi.org/10.1109/TGRS.2015.2505677, 2016.

Long, D. G., and Daum, D. L.: Spatial resolution enhancement of SSM/I data, IEEE Trans. Geosci. Remote Sens., 36, 407-417, https://doi.org/10.1109/36.662726, 1998.

Long, D. G., and Drinkwater, M. R.: Greenland Ice Sheet surface properties observed by the Seasat-A scatterometer at enhanced resolution, J. Glaciol., 40, 213-230, https://doi.org/10.1017/S0022143000007310, 1994.

Long, D. G., Hardin, P. J., and Whiting, P. T.: Resolution enhancement of spaceborne scatterometer data, IEEE Trans. Geosci. Remote Sens., 31, 700-715, https://doi.org/10.1109/36.225536, 1993.

MacFerrin, M., Machguth, H., van As, D., Charalampidis, C., Stevens, C. M., Heilig, A., Vandecrux, B., Langen, P. L., Mottram, R., Fettweis, X., van den Broeke, M. R., Pfeffer, W. T., Moussavi, M. S., and Abdalati, W.: Rapid expansion of Greenland's low-permeability ice slabs. Nature, 573, 403-407, https://doi.org/10.1038/s41586-019-1550-3, 2019.

Machguth, H. McFerrin M., van As, D., Box, J. E., Charalampidis, C., Colgan., W., Fausto, R. S., Harro, A. J., Mosley-Thompson, E., and van de Wal, R. S. W.: Greenland meltwater storage in firn limited by near-surface ice formation. *Nat. Clim. Chang*. 6, 390-393, https://doi.org/10.1038/nclimate2899, 2016.

Mätzler, C., and Hüppi, R.: Review of signature studies for microwave remote sensing of snowpacks, Adv. in Space Res., 9, 253-265, https://doi.org/10.1016/0273-1177(89)90493-6, 1989.

Miège, C., Forster, R. R., Brucker, L., Koenig, L. S., Solomon, D.K., Paden, J. D., Box, J. E., Burgess, E. W., Miller, J. Z., McNerney, L., Brautigam, N., Fausto, R. S., and Gogineni, S.: Spatial extent and temporal variability of Greenland firn aquifers detected by ground and airborne radars, J. Geophys. Res. Earth, 121, 2381–2398, https://doi.org/10.1002/2016JF003869, 2016.

Miles, K. E., Willis, I. C., Benedek, C. L., Williamson, A. G., and Tedesco, M.: Toward monitoring surface and subsurface lakes on the Greenland Ice Sheet Using Sentinel-1 SAR and Landsat-8 OLI imagery, Frontiers in Earth Science, 5, 58, https://doi.org/https://doi.org/10.3389/feart.2017.00058, 2017.

Miller, J. Z., Long, D. G., Jezek, K. C., Johnson, J. T., Brodzik, M. J., Shuman, C. A., Koenig, L. S., and Scambos, T. A.: Brief communication: Mapping Greenland's perennial firn aquifers using enhanced-resolution L-band brightness temperature image time series, The Cryosphere, 14, 2809–2817, https://doi.org/10.5194/tc-14-2809-2020, 2020.

Miller, J. Z.: Mapping Greenland’s firn aquifers from space using active and passive satellite microwave remote sensing, Ph.D. thesis, Department of Geography, University of Utah, 135 pp., 2019.

Miller, O. L., Solomon, D. K., Miège, C., Koenig, L. S., Forster, R. R., Montgomery, L. N., Schmerr, N., Ligtenberg, S. R. M., Legchenko, A., and Brucker, L.: Hydraulic conductivity of a firn aquifer in southeast Greenland, Front. Earth Sci., 5, https://doi.org/10.3389/feart.2017.00038, 2017.

Montgomery, L. N., Schmerr, N., Burdick, S., Forster, R. R., Koenig, L., Legchenko, A., Ligtenberg, S., Miège, C., Miller, O. L., and Solomon, D. K.: Investigation of firn aquifer structure in southeastern Greenland using active source seismology, Front. Earth Sci., 5, https://doi.org/10.3389/feart.2017.00010, 2017.

Moon, T., Joughin, I., Smith, B., Broeke, M. R., Berg, W. J., Noël, B., and Usher, M.: Distinct patterns of seasonal Greenland glacier velocity, Geophys. Res. Lett., 41, 7209-7216, https://doi.org/10.1002/2014GL061836, 2014.

Mote, T. L., and Andersen, M. R.: Variations in snowpack melt on the Greenland Ice Sheet based on passive microwave measurements, J. Glaciology, 41, 51-60, https://doi.org/10.1017/S0022143000017755, 1995.

Noël, B., van Kampenhout, L., Lenaerts, J. T. M., van de Berg, W. J, and van den Broeke, M. R.: A 21st century warming threshold for sustained Greenland Ice Sheet mass loss, Geophys. Res. Lett.,, 48(5), https://doi.org/10.1029/2020GL090471, 2021.

Noël, B., van de Berg, Willem Jan, Lhermitte, S. L. M., and van den Broeke, Michiel R.: Rapid ablation zone expansion amplifies north Greenland mass loss, Sci. Adv, 5, eaaw0123, https://doi.org/10.1126/sciadv.aaw0123, 2019.

Noël, B., van de Berg, W. J., van Wessem, J. M., van Meijgaard, E., van As, D., Lenaerts, J. T. M., Lhermitte, S., Kuipers Munneke, P., Smeets, C. J. P. P., van Ulft, L. H., van de Wal, R. S. W., and van den Broeke, M. R.: Modelling the climate and surface mass balance of polar ice sheets using RACMO2 – Part 1: Greenland (1958–2016), The Cryosphere, 12, 811–831, https://doi.org/10.5194/tc-12-811-2018, 2018.

https://doi.org/10.5194/tc-2021-116
Preprint. Discussion started: 30 April 2021

Nghiem, S. V., Hall, D. K., Mote, T. L., Tedesco, M., Albert, M. R., Keegan, K., Shuman, C. A., DiGirolamo, N. E., & Neumann, G.: The extreme melt across the Greenland Ice Sheet in 2012, Geophys. Res. Lett.,, 39, https://doi.org/10.1029/2012GL053611, 2003

Nghiem, S. V., Hall, D. K., Mote, T. L., Tedesco, M., Albert, M. R., Keegan, K., Shuman, C. A., DiGirolamo, N.E., and Neumann, G.: The extreme melt across the Greenland Ice Sheet in 2012, Geophys. Res. Lett., 39, L20502, https://doi.org/10.1029/2012GL053611, 2012.

Paden, J., Li, J., Leuschen C., F. Rodriguez-Morales, F., and Hale, R.: IceBridge Accumulation Radar L1B Geolocated Radar Echo Strength Profiles, Version 2, NASA National Snow and Ice Data Center Distributed Active Archive Center, https://doi.org/10.5067/0ZY1XYHNIQNY, 2014, updated 2018.
Partington, K. C.: Discrimination of glacier facies using multi-temporal SAR data. J. Glaciol., 44, 42-53. https://doi.org/10.3189/S0022143000002331, 1998.

Pfeffer, W. T., Meier, M. F., and Illangasekare, T. H.: Retention of Greenland runoff by refreezing: Implications for projected future sea level change. J. Geophys. Res. Oceans, 96, 22117-22124, https://doi.org/10.1029/91JC0250, 1991.

Pfeffer, W. T., and Humphrey, N.F.: Determination of timing and location of water movement and ice-layer formation by temperature measurements in sub-freezing snow, J. Glaciol., 42, 292-304, https://doi.org/10.1017/S0022143000004159, 1996.

Piepmeier, J. R., et al.: SMAP L-band microwave radiometer: Instrument design and first year on orbit. IEEE Trans. Geosci. Remote Sens, 55, 1954-1966, https://doi.org/10.1109/TGRS.2016.2631978, 2017.

Poinar, K., Joughin, I., Lilien, D., Brucker, L., Kehrl, L., and Nowicki, S.: Drainage of southeast Greenland firn aquifer water through crevasses to the bed. Front. Earth Sci., https://doi.org/10.3389/feart.2017.00005, 2017.

Poinar, K., Dow, C. F., and Andrews, L. C.: Long-term support of an active subglacial hydrologic system in southeast Greenland by firn aquifers. Geophys. Res. Lett., 46, 4772-4781, https://doi.org/10.1029/2019GL082786, 2019.

Rignot, E.: Backscatter model for the unusual radar properties of the Greenland Ice Sheet, J. Geophys. Res. Planets, 100, 9389–9400, https://doi.org/10.1029/95JE00485, 1995.

Rignot, E. J., Ostro, S. J., Van Zyl, J., and Jezek, K. C.: Unusual radar echoes from the Greenland Ice Sheet, Science, 261, 1710-1713, https://doi.org/10.1126/science.261.5129.171, 1993.

Rodriguez-Morales, F., et al.: Advanced multi-frequency radar instrumentation for polar research, IEEE Trans. Geosci. Remote Sens., 52, 2824-2842, https://doi.org/10.1109/TGRS.2013.2266415, (2014).

Schröder L., Neckel N., Zindler R., Humbert A.: Perennial supraglacial lakes in northeast Greenland observed by polarimetric SAR, Remote Sensing, 12, 2798, https://doi.org/10.3390/rs12172798 (2020).

Shuman, C. A., Hall, D. K., DiGirolamo, N. E., Mefford T. K., and Schnaubelt, M. J.: Comparison of near-surface air temperatures and MODIS ice-surface temperatures at Summit, Greenland (2008–2013), J. Appl. Meteor. Climatol., 53, 2171-2180, https://doi.org/10.1175/JAMC-D-14-0023.1, 2014.

Steffen, K., Nghiem, S. V., Huff, R., and Neumann, G.: The melt anomaly of 2002 on the Greenland Ice Sheet from active and passive microwave satellite observations. Geophys. Res. Lett., 31, L2040, https://doi.org/10.1029/2004GL020444, 2004.

Stevens, L. A., Behn, M. D., McGuire, J. J., Das, S. B., Joughin, I., Herring, T., Shean, D. E., and King, M. A.: Greenland supraglacial lake drainages triggered by hydrologically induced basal slip, Nature, 522, 73-76. https://doi.org/10.1038/nature14480, 2015.

Swift, C. T., Hayes, P. S., Herd, J. S., Jones, W. L., and Delnore, V. E.: Airborne microwave measurements of the southern Greenland Ice Sheet, J. Geophys. Res. Solid Earth, 90, 1983-1994, https://doi.org/10.1029/JB090iB02p01983, 1985.

Tedesco, M., and Fettweis, X.: Unprecedented atmospheric conditions (1948–2019) drive the 2019 exceptional melting season over the Greenland Ice Sheet, The Cryosphere, 14, 1209-1223, https://doi.org/10.5194/tc-14-1209-2020, 2020.

Tedesco, M., Mote, T., Fettweis, X., Hanna, E., Jeyaratnam, J., Booth, J. F., Datta, R., and Briggs, K.: Arctic cut-off high drives the poleward shift of a new Greenland melting record, Nature Commun., 7, 11723-11723, https://doi.org/10.1038/ncomms11723 1985, 2016.

Tedesco, M., Fettweis, X., van den Broeke, M. R., van de Wal, R. S. W., Smeets, C. J. P. P., van de Berg, W. J., Serreze, M. C., and Box, J. E.: The role of albedo and accumulation in the 2010 melting record in Greenland, Environ. Res. Lett, 6, 014005, https://doi.org/10.1088/1748-9326/6/1/014005, 2011.

Tedesco, M., Serreze, M., and Fettweis, X.: Diagnosing the extreme surface melt event over southwestern Greenland in 2007. The Cryosphere, 2, 159-166. https://doi.org/10.5194/tc-2-159-2008, 2008.

Tiuri, M. E., Sihvola, A. H., Nyfors, E. G., Hallikaiken, M. T.: The complex dielectric constant of snow at microwave frequencies, IEEE J. Ocean Eng, 9, 377-382, https://doi.org/10.1109/JOE.1984.1145645, 1984.

Tsai, W., Nghiem, S. V., Van Zyl, J. J.: SeaWinds scatterometer on QuikSCAT mission and the emerging land and ocean applications, Proc. SPIE 4152, https://doi.org/10.1117/12.410586, 2000.

Trusel, L. D., Das, S. B., Osman, M. B., Evans, M. J., Smith, B. E., Fettweis, X., McConnell, J. R., Noël, B. P. Y., and van den Broeke, M. R.: Nonlinear rise in Greenland runoff in response to post-industrial Arctic warming, Nature, 564, 104-108, https://doi.org/10.1038/s41586-018-0752-4, 2018.

Turton, J. V., Hochreuther, P., Reimann, N., and Blau, M. T.: The distribution and evolution of supraglacial lakes on the 79° N Glacier (northeast Greenland) and interannual climatic controls, The Cryosphere Discuss, https://doi.org/10.5194/tc-2021-45, in review, 2021.

Ulaby, F. T., Long, D. G., Blackwell, W. J., Elachi, C., Fung, A. K., Ruf, C., Sarabandi, C., Zebker, H. A., Van Zyl, J.: Microwave radar and radiometric remote sensing, University of Michigan Press, Ann Arbor, 2014.

van den Broeke, M. R., Enderlin, E. M., Howat, I. M., Kuipers Munneke, P., Noël, B. P. Y., van de Berg, W. J., van Meijgaard, E., and Wouters, B.: On the recent contribution of the Greenland ice sheet to sea level change, The Cryosphere, 10, 1933–1946, https://doi.org/10.5194/tc-10-1933-2016, 2016.

van der Veen, C. J.: Fracture propagation as means of rapidly transferring surface meltwater to the base of glaciers, Geophys. Res. Lett., 34, L01501, https://doi.org/10.1029/2006GL028385, 2005.

Wessel, P., and Smith, W. H. F.: A global, self-consistent, hierarchical, high-resolution shoreline database, J. Geophys. Res., 101, 8741–8743, https://doi.org/10.1029/96JB00104, 1996.

Zabel, I. H. H., Jezek, K. C., Baggeroer, P. A., and Gogineni, S. P: Ground-based radar observations of snow stratigraphy and melt processes in the percolation facies of the Greenland Ice Sheet, Ann. Glaciol., 21, 40-44. https://doi.org/10.3189/S0260305500015573, 1995.

https://doi.org/10.5194/tc-2021-116
Preprint. Discussion started: 30 April 2021

The Cryosphere Discussions
Open Access
EGU

Zwally, H. J., Abdalati, W., Herring, T., Larson, K., Saba, J., and Steffen, K.: Surface melt-induced acceleration of Greenland Ice Sheet flow, Science, 297, 218-222, https://doi.org/10.1126/science.1072708, 2002.

Zwally, J. H.: Microwave emissivity and accumulation rate of polar firn, J. Glaciol., 18, 195-215, https://doi.org/10.1017/S0022143000021304, 1977.